What Controls the Interannual Variability of the Boreal Winter Atmospheric River Activities over the Northern Hemisphere?

Weiming Ma,[a] Gang Chen[a]

[a] *Department of Atmospheric and Oceanic Sciences, University of California, Los Angeles, Los Angeles, California*

Corresponding author: Weiming Ma, mawei@atmos.ucla.edu

File generated with AMS Word template 2.0

Early Online Release: This preliminary version has been accepted for publication in *Journal of Climate* cited, and has been assigned DOI 10.1175/JCLI-D-22-0089.1. The final typeset copyedited article will replace the EOR at the above DOI when it is published.

ABSTRACT

Interannual variability of the winter AR activities over the Northern hemisphere is investigated. The leading modes of AR variability over the North Pacific and North Atlantic are first identified and characterized. Over the Pacific, the first mode is characterized by a dipole structure with enhanced AR frequency along the AR peak region at about $30^{\circ}N$ and reduced AR frequency further north. The second mode exhibits a tri-pole structure with a narrow band of positive AR anomalies at about $30^{\circ}N$ and sandwiched by negative anomalies. Over the Atlantic, the first mode exhibits an equatorward shift of the ARs with positive anomalies and negative anomalies located on the equatorward and poleward side of the AR peak region at about $40^{\circ}N$, respectively. The second mode is associated with the strengthening and eastward extension of the AR peak region which is sandwiched by negative anomalies. A large ensemble of atmospheric global climate models from the Coupled Model Intercomparison Project phase 6 (CMIP6), which shows high skills in simulating these modes, is then used to quantify the roles of sea surface temperature (SST) forcing versus internal atmospheric variability in driving the formation of these modes. Results show that SST forcing explains about half of the variance for the Pacific leading modes, while that number drops to about a quarter for the Atlantic leading modes, suggesting higher predictability for the Pacific AR variability. Additional ensemble driven only by observed tropical SST is further utilized to demonstrate the more important role that tropical SST plays in controlling the Pacific AR variability while both tropical and extratropical SST exert comparable influences on the Atlantic AR variability.

1. Introduction

Atmospheric rivers (ARs), defined as filaments of intense moisture transport in the atmosphere, exert profound impacts on the global hydrological cycle and regional weather extremes. Despite covering only about 10% of the latitude circumference in the midlatitudes at any given time, it is estimated that they are responsible for more than 90% of the poleward moisture transport (Zhu and Newell 1998). ARs are important water suppliers for many regions around the world. On the one hand, they contribute significantly to the annual total precipitation to regions, such as the North American west coast, western Europe and Southern South America (Dettinger et al. 2011; Rutz and Steenburgh 2012; Lavers and Villarini 2015; Viale et al. 2018). For example, it is estimated that California receives up to 50% of its annual total precipitation from ARs (Dettinger et al. 2011). On the other hand,

Accepted for publication in *Journal of Climate*. DOI 10.1175/JCLI-D-22-0089.1.

they are also responsible for many weather extremes, such as extreme precipitation (Lavers and Villarini 2013; Leung and Qian 2009; Lamjiri et al. 2017; Ma et al. 2020b), extreme wind events (Waliser and Guan 2017) and rain-on-snow events (Guan et al. 2016; Bozkurt et al. 2021; McGowan et al. 2021). Recently, their presences in the tropics and the polar regions are also starting to get recognized (Woods and Caballero 2016; Mattingly et al. 2018; Nash et al. 2018; Thapa et al. 2018; Francis et al. 2020). ARs play complex roles in influencing the polar climate. Studies show that ARs can induce sea ice losses and ice sheet melting (Mattingly et al. 2018; Woods and Caballero 2016), but they can also cause anomalous snow accumulation (Gorodetskaya et al. 2014). With ARs shifting poleward in both the present and future climate (Zhang et al. 2021; Gao et al. 2016; Ma et al. 2020a), it's likely that ARs will exert stronger influences on the polar climate.

Considering the important roles that ARs play in the climate system, it is critical for both disaster preparation and water resource management to understand what controls their variability for timescales ranging from subseasonal-to-seasonal (S2S) to interannual. At the S2S timescale, Madden-Julian Oscillation (MJO) provides the dominant source of predictability for AR activities over the North Pacific (Guan et al. 2012; Zhou et al. 2021), but its role is also modulated by the Quasi-biennial Oscillation (QBO) (Mundhenk et al. 2018; Baggett et al. 2017). By analyzing six decades of observed data, Guirguis et al. (2019) find that Arctic Oscillation, Eastern Pacific Oscillation and Western Pacific Oscillation strongly modulate subseasonal AR activities over Northern California, for which Northern California tends to receive more precipitation during boreal winter when these modes are in their negative phase. At the interannual timescale, Gershunov et al. (2017) find that landfalling ARs over the western North America during boreal winter are modulated by the Pacific Decadal Oscillation and the "blob" of warm SST off the Pacific Northwest (Bond et al. 2015). ENSO, as the dominant mode of SST variability at the interannual timescale, has also been shown to exert strong influences on the AR landfalls along the North American west coast, with such influences being dependent on the ENSO flavors (Kim et al. 2017; Xiong and Ren 2021).

While ENSO can provide predictability for AR activities at the interannual timescale, internal atmospheric variability, which is intrinsic to the atmosphere, can also strongly modulate AR variability (Teng and Branstator 2017; Zhang et al. 2018; Dong et al. 2018; Kumar and Chen 2017; Chen and Kumar 2018; Deser et al. 2018; Cash and Burls 2019). One

Accepted for publication in *Journal of Climate*. DOI 10.1175/JCLI-D-22-0089.1.

of such examples is the well-known failed 2016 winter rains in Southern California. The winter of 2015/16 was associated with a major El Nino event with magnitude comparable to the 1997/98 event. Historically, strong El Nino events tend to cause wet rainy seasons over California. This led to heightened expectations that the multi-year drought that California was experiencing at that time would finally be alleviated in 2016. However, the anticipated high rainfall in Southern California did not materialize that winter, leaving the drought continuing into 2017. A later modelling study suggests that this failed rainfall is not a response to the boundary forcing and attributes the cause to internal atmospheric variability (Zhang et al. 2018). Indeed, using a large ensemble of models from the Atmospheric Model Intercomparison Project (AMIP) participated in CMIP5 (Taylor et al. 2012), Dong et al. (2018) shows that about 80% of the interannual variability of winter precipitation in California is controlled by internal atmospheric variability. However, this view has been challenged recently. Using the newly defined ENSO Longitude Index, Patricola et al. (2020) argues that the failed 2016 winter rains in Southern California can be explained by the spatial pattern of the El Nino, rather than internal atmospheric variability. Given such complex interplay between the SST forcing and internal atmospheric variability in modulating AR and precipitation variability, a natural question to ask is what relative roles SST forcing versus internal atmospheric variability play in driving the interannual AR variability.

In this study, we will address the question posed above for the winter AR variability over the Northern hemisphere. To the best of our knowledge, only few studies have focused on the leading modes of winter AR variability over the North hemisphere so far, but the AR response to climate forcing is often dominated by the leading modes of low frequency variability. For example, by applying empirical orthogonal function (EOF) analysis to the integrated water vapor transport (IVT) field induced by ARs, Dong et al. (2018) identifies the two leading modes of winter AR variability over the North Pacific. They show that the first mode correlates strongly with the interannual variability of extreme precipitation along the U.S. west coast. Over the North Atlantic, Li et al. (2022) identifies the first three modes of SST-forced winter AR variability using a 30-member ensemble of AMIP-style simulations. They also identify the large-scale climate modes behind these leading modes. In the first part of this study, we will first systematically identify and characterize the leading modes of interannual AR variability in the North Pacific and North Atlantic during winter in observation. A large ensemble of AMIP-type models from CMIP6 is then evaluated on their performance in simulating these modes (Eyring et al. 2016). After showing that these models

Accepted for publication in *Journal of Climate*. DOI 10.1175/JCLI-D-22-0089.1.

are capable of producing AR climatology and variability with high fidelity, we systematically quantify the roles of SST forcing versus internal atmospheric variability in driving the interannual variability of these modes. For the forced component of AR variability, the relative roles of tropical SST versus extratropical SST are also explored.

This paper is structured as follows. In section 2, we will first describe the observed datasets and the model datasets. We will then describe the AR detection algorithm and the EOF method used to extract the leading modes of AR frequency anomalies in observation. The singular value decomposition (SVD) method used to derive the leading modes of AR anomalies for the covariance between observation and models is also described in this section. Major findings will be presented in sections 3 and 4. A brief conclusion will be provided in section 5.

2. Data and method

a. Observations and model datasets

This study focuses on the Northern Hemisphere winter season (December, January and February (DJF)) from 1979 to 2014, which covers the longest overlapping period between the observations and model datasets. The observed AR statistics are based on the daily mean of the 6-hourly horizontal winds and specific humidity at 1000, 850, 700 and 500 mb levels from the ECMWF Interim reanalysis (ERA-Interim) (Dee et al. 2011) with spatial resolution of $1.5^{\circ} \times 1.5^{\circ}$. The detrended winter AR frequency anomalies are used to define the leading modes of AR variability on the interannual timescale, to be described in section 2c. Monthly sea level pressure from ERA-Interim is used to characterize the large-scale circulation associated with the leading modes of AR variability. Daily precipitation covering the period from 1996 to 2014 from Global Precipitation Climatology Project (GPCP) (Huffman et al. 2001) is used to examine the winter mean and extreme precipitation anomalies associated with the leading modes of AR variability. In this study, the winter mean precipitation is defined as the total precipitation summed over all the daily precipitation during winter. Extreme precipitation is defined as the total precipitation summed over all the winter days with daily precipitation exceeding the 95th percentile of the winter daily precipitation. To test the robustness of the results, we also examine the daily precipitation calculated from the 12-hour accumulated precipitation from ERA-Interim, which covers the entire study period. The

Accepted for publication in *Journal of Climate*. DOI 10.1175/JCLI-D-22-0089.1.

observed SST is from the Hadley Centre Sea Ice and Sea Surface temperature dataset (HadISST) (Rayner et al. 2003).

AMIP models driven by observed changes in SST and sea ice are useful tools to study how boundary forcing drives the observed interannual variability of the atmosphere. To quantify the contributions of the SST/sea ice forcing versus the internal atmospheric variability in driving the interannual variability in ARs, a large ensemble of AMIP-type models participated in CMIP6 (i.e., 30 AMIP6 models) are used in this study. Some of the models contain more than one ensemble member, but only the first member with the tag "r1i1p1f1" is used. Details on the models' name, institution, horizontal resolution and the number of ensemble members used for each model are described in Table S1. Similar to ERA-Interim, daily horizontal winds and specific humidity at 1000, 850, 700 and 500 mb in the AMIP datasets are used to calculate the AR statistics.

In addition, we examine another model ensemble by including nine additional members for four of the models in the AMIP ensemble (i.e., ACCESS-ESM, CESM2, IPSL and MIROC6), making the ensemble size of each of these four models to be ten. We repeat the analysis with this 40-member ensemble. The results based on this 40-member ensemble (not shown) are very similar to those based on the 30-member ensemble described in the previous paragraph. Therefore, only the results based on the 30-member ensemble are presented here except for Figs. 6 and 7.

Two additional ensembles from the CESM1 are also employed to investigate the roles of tropical SST versus extratropical SST in driving the AR variability. Similar to the AMIP models described above, one ensemble, which consists of 10 members, is driven by the observed global SST and sea ice and is termed "Global Ocean Global Atmosphere" (GOGA). Another ensemble, which also consists of 10 members, is driven by the observed SST only in the tropical ocean from $28^{\circ}S$ to $28^{\circ}N$ and climatological SST poleward of 35°. A linear interpolation zone is set between 28° and 35°. This ensemble is termed "Tropical Ocean Global Atmosphere" (TOGA). Daily horizontal winds and specific humidity at the lowest model level, 850, 500 and 200 mb are used to calculate AR statistics for these two ensembles.

b. AR detection algorithm

We employ the IVT-based AR detection algorithm developed by Guan and Waliser (2015). This algorithm detects ARs globally and is shown to compare favorably with other AR detection algorithms (Guan and Waliser 2015). Many criteria, which are commonly used

Accepted for publication in *Journal of Climate*. DOI 10.1175/JCLI-D-22-0089.1.

in other AR detection algorithms, are also employed in this algorithm, but the global algorithm used here helps identify large-scale AR activity patterns rather than local features. We will outline the major steps taken by this algorithm to detect ARs here. Readers are referred to Guan and Waliser (2015) for a more detailed description of the algorithm. Our analysis focuses on the winter mean AR frequency, which is defined as the fraction of time a grid point experiences AR condition in a given winter.

This algorithm first identifies contiguous regions of elevated IVT ("objects") based on the seasonally and regionally dependent 85th percentile of IVT magnitude or 100 kg m^{-1} s^{-1}, whichever is larger. To ensure coherence of the detected object, at least half of the grids of the object should have the IVT direction within 45° of the object mean IVT direction. Since ARs are important for poleward moisture transport, the detected object is required to exhibit a mean poleward IVT of at least $50\ kg\ m^{-1}s^{-1}$. A detected AR should also be longer than 2000 km and with a length-to-width ratio greater than 2. IVT is calculated by vertically integrating the moisture flux from the lowest vertical level to the highest vertical level using the 4 levels available for each dataset. The IVT threshold is calculated by using the entire study period of each individual dataset. Since this algorithm detects ARs based on a percentile threshold, the results in this study are not sensitive to the different vertical levels used among datasets (not shown).

c. Analysis Methods

EOF analysis is used to identify the leading modes of winter AR frequency anomalies over the North Pacific and North Atlantic, with the frequency weighted by the square root of the cosine of latitude. Following Barnes and Polvani (2013) and Ma et al. (2021), North Pacific and North Atlantic are defined as the regions from 0 to $90^{\circ}N$ and $135^{\circ}E$ to $125^{\circ}W$, from 0 to $90^{\circ}N$ and $60^{\circ}W$ to 0, respectively. Shifting the boundaries of these defined regions in either direction for a few degrees would not affect the results shown in this study. To evaluate the performance of AMIP models on simulating the leading modes in winter AR variability, centered pattern correlation is used to measure the spatial pattern similarity between the modes identified in observation and those derived from AMIP models. As we will show later, AMIP models generally show high skills in reproducing these leading modes, but biases still exist.

To quantify the contributions of SST/sea ice forcing versus internal atmospheric variability in the interannual variability of the observed leading modes, a combined SVD

Accepted for publication in *Journal of Climate*. DOI 10.1175/JCLI-D-22-0089.1.

analysis (Wallace et al. 1992; Bretherton et al. 1992) between observation and AMIP ensemble is used in this study. Following Mori et al. (2019), SVD analysis of the covariance matrix of winter AR frequency anomalies between observation and simulations is used to derive the leading modes of interannual AR variability. The spatial patterns derived from this covariance method are quantitively similar to those from the EOF analysis that is based on the variance of observations or individual simulations. But the leading modes obtained from this covariance method would explain the maximum squared temporal covariances between the observation and simulations over the analysis domains.

To carry out the SVD analysis, we first regrid all detrended winter AR frequency anomalies relative to their own climatology to a common spatial resolution of $1.5^{\circ} \times 1.5^{\circ}$. This can ensure that both observation and simulations have the same spatial dimension. A covariance matrix is then constructed between the observed AR anomalies and the simulated AR anomalies. More specifically, 30 members, one from each of the 30 AMIP models, are concatenated in the time dimension to form a matrix with time dimension size of 1050 (35 winters x 30 members, the row dimension).

$$M = \begin{bmatrix} model_1 & \cdots & model_{30} \\ \vdots & \ddots & \vdots \\ \vdots & \cdots & \vdots \end{bmatrix}$$

To match the time dimension size of 1050 in the simulations, we duplicate the observed time series 30 times to form a matrix for the observed anomalies.

$$O = \begin{bmatrix} observation & \cdots & observation \\ \vdots & \ddots & \vdots \\ \vdots & \cdots & \vdots \end{bmatrix}$$

The product of the two matrices along the time dimension forms a covariance matrix on which we carry out the SVD analysis (Eq. 1).

$$Cov[observation, models] = \frac{1}{1050 - 1}(OM^T) \tag{1}$$

The left and right singular vectors derived from this covariance matrix with largest singular values depict the spatial patterns of the leading modes of interannual winter AR variability in observation and simulations, respectively. The associated expansion coefficients (ECs) are obtained by projecting the detrended winter AR frequency anomalies onto the singular vectors, giving the time series for the 35-winter period in observation (also duplicates 30 times) and simulations in each ensemble member.

Accepted for publication in *Journal of Climate*. DOI 10.1175/JCLI-D-22-0089.1.

As will be shown in Figure 5, we evaluate models' skill in simulating AR variability which is defined as the standard deviation of winter AR frequency.

$$std(f)$$

where f is the time series of winter AR frequency for a mode with dimension of 35 (i.e. 35 winters). We further decompose the AR variability in models into a forced component driven by boundary forcing:

$$forced\ variability = std(\bar{f})$$

where $\bar{f}$ is the ensemble mean time series of winter AR frequency, and an internal variability component:

$$internal\ variability = \frac{1}{35}(\sum_{y=1}^{35} std(f_{all}^{y} - \bar{f}^{y}))$$

where y denotes the winter of the y^{th} year and all represents all models. For example, f_{all}^{1} represents the AR frequency of the 1st winter (i.e. 1980) of all models (i.e. 30).

3. Observed EOF modes and model evaluations

a. The observed leading modes of winter AR variability based on EOF analysis

Figure 1 shows the observed leading EOF modes of winter AR anomalies over the North Pacific and the associated anomalies of sea level pressure, IVT, 850 mb zonal wind and integrated water vapor (IWV). The positive phase of the EOF mode is defined such that the anomalous AR frequency is enhanced over the U.S. west coast. The first mode is characterized by enhanced AR frequency over the AR maximum region and reduced AR activities further north (Fig. 1a). The spatial pattern of this mode is very similar to the first mode of the North Pacific winter AR variability based on AR IVT identified in Dong et al. (2018) (see their Fig 3c). The band of enhanced AR frequency extends northeastward and depicts higher than normal AR frequency along the North American west coast, especially along the U.S west coast. The associated sea level pressure anomaly pattern shows a low anomaly over the northeast Pacific, indicating southeastward shift of the Aleutian low (Fig. 1c). This low anomaly induces a cyclonic pattern in the IVT anomalies and enhances onshore IVT toward the west coast of North America. In agreement with the presence of a low anomaly over the northeast Pacific, the 850 mb zonal wind strengthens and extends eastward

File generated with AMS Word template 2.0

Accepted for publication in *Journal of Climate*. DOI 10.1175/JCLI-D-22-0089.1.

on the equatorward side of the climatological jet and weakens on the poleward side (Fig. 1e). This associated wind anomaly pattern also bears strong resemblance to the first EOF mode of 850 mb zonal wind anomalies over the Pacific (Fig. S1). Indeed, the principal component (PC) associated with AR variability correlates significantly with the PC of the 850mb zonal wind anomalies with correlation coefficient of 0.78. This implies that the interannual variability in ARs is mostly controlled by the variability in circulation. Moreover, the associated IWV shows positive anomalies over the eastern Pacific near/along the North American west coast (Fig. 1g). Both the positive anomalies in wind and IWV contribute to enhanced AR frequency along the North American west coast. Further away from the eastern Pacific, negative IWV anomalies are seen nearly everywhere, even over regions with enhanced AR frequency. This again suggests a stronger role wind variability plays in regulating the AR variability.

The second mode depicts a narrow band of slightly enhanced AR frequency poleward of the AR maximum region, accompanied by negative AR anomalies on both sides of this positive AR anomaly (Fig. 1b). This mode also shows strong similarity to the second mode of the North Pacific winter AR variability in Dong et al. (2018) (see their Fig. 3f). The associated sea level pressure anomaly pattern shows a high anomaly over the central subtropical Pacific and a low anomaly over the northeast Pacific (Fig. 1d). This dipole pattern in sea level pressure resembles the North Pacific Oscillation (Rogers 1981). Compared to the 1st mode, the low anomaly is shifted northward and weaker in intensity (Fig. 1d and 1c), resulting in weaker IVT anomalies directed toward the northwestern U.S. and British Columbia. . Consistent with the sea level pressure anomalies, the associated wind anomalies show strengthening and eastward extension of the jet (Fig. 1f). Since there is no significant IWV anomaly over the region off the west coast (Fig. 1h), the enhanced AR frequency there is mostly due to the strengthening of the winds.

Accepted for publication in *Journal of Climate*. DOI 10.1175/JCLI-D-22-0089.1.

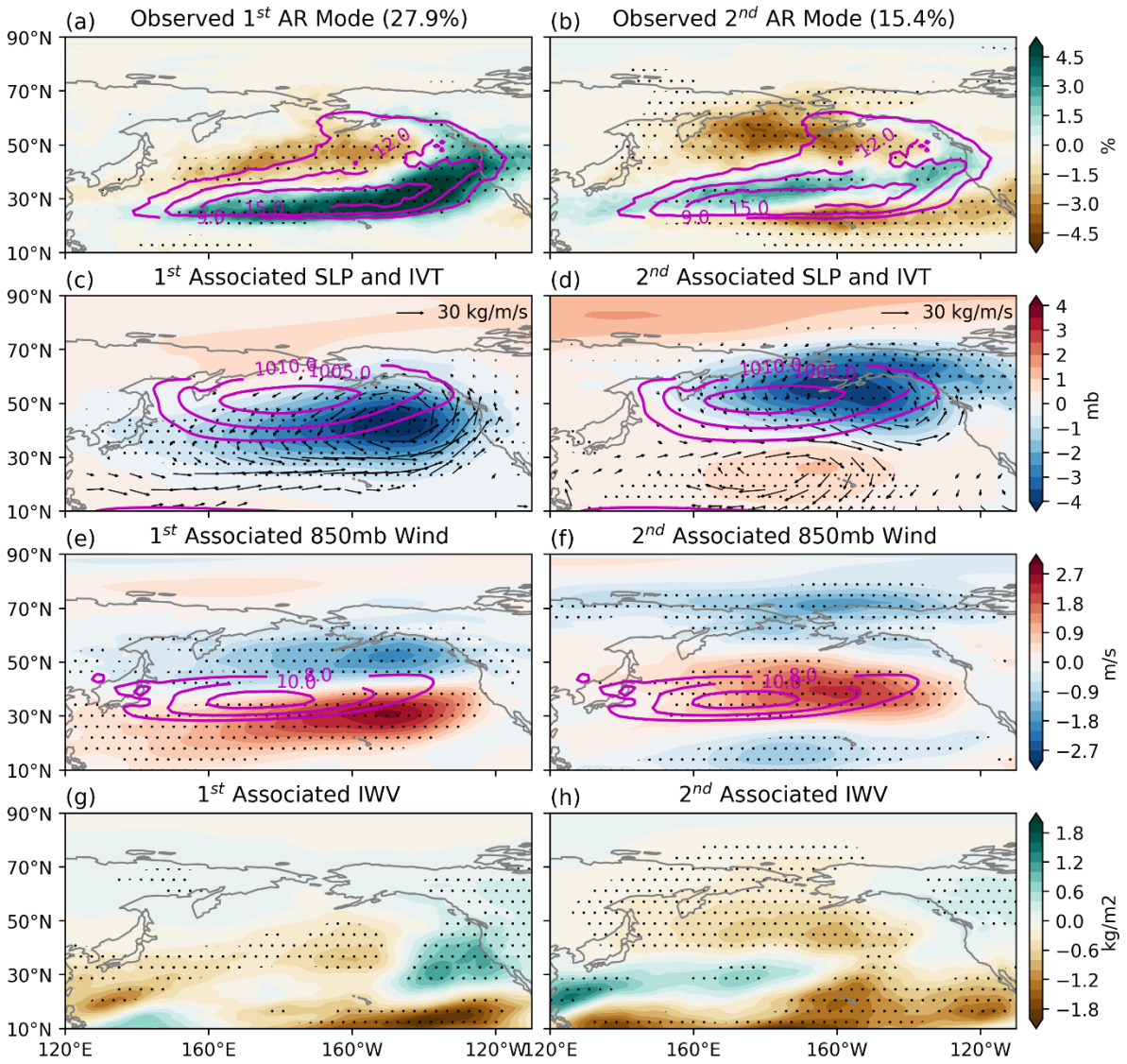

Figure 1. Observed AR frequency anomalies (a), (b), sea level pressure and IVT anomalies (c), (d), 850 mb zonal wind anomalies (e), (f), IWV anomalies (g), (h) associated with the first and second EOF modes of winter AR anomalies over the North Pacific, respectively. The values (i.e., 27.9% and 15.4%) in the title of (a) and (b) indicate the percentage of variance explained by each EOF. Patterns are the regression coefficients obtained by regressing their anomaly fields onto the respective standardized principal components (PCs) (i.e., linear regression between the time series of the anomaly fields and the time series of the standardized PCs). Solid contours in (a), (b), (c), (d), (e) and (f) indicate the climatology of the respective field. Shaded contours show the anomalies. Stippling indicates regions with anomalies significant at 95% confidence level based on Student's t test.

Since ARs contribute significantly to both the mean and extreme precipitation for many regions around the world, Figure 2 displays the mean and extreme precipitation patterns

Accepted for publication in *Journal of Climate*. DOI 10.1175/JCLI-D-22-0089.1.

associated with these leading AR modes. Consistent with the AR anomaly pattern (Fig. 1a), the first mode is associated with both enhanced mean and extreme precipitation over the eastern Pacific and along the U.S west coast (Fig. 2a and 2c). Reduced mean and extreme precipitation are found over the central north Pacific from about $30^{\circ}N$ to $50^{\circ}N$. Significant anomalies are also found in the tropics south of $20^{\circ}N$, where no significant AR anomaly is found. Since most of the tropical precipitation is controlled by convective activities rather than ARs that are typically associated with cold fronts, significant precipitation anomalies over these latitudes likely result from the anomalies of these non-AR weather systems which covary with the AR mode. As shown in Figure 2b, the mean precipitation anomalies associated with the second mode show a band of enhanced precipitation over regions at around $40^{\circ}N$ stretching across the Pacific from about 180° to the coast of northwest U.S. Significant negative precipitation anomalies are also found over the coastal regions of northwest Pacific and central Pacific equatorward of the positive precipitation band. The negative anomalies over these regions are also significant for the extreme precipitation (Fig. 2d). Note that the GPCP covers a relatively short period. To test the robustness of the results, precipitation from ERA-Interim, which covers the whole period, is used to reproduce the above results. The anomaly patterns based on ERA-Interim are very similar to those based on GPCP, further corroborating the robustness of the results (Fig. S2).

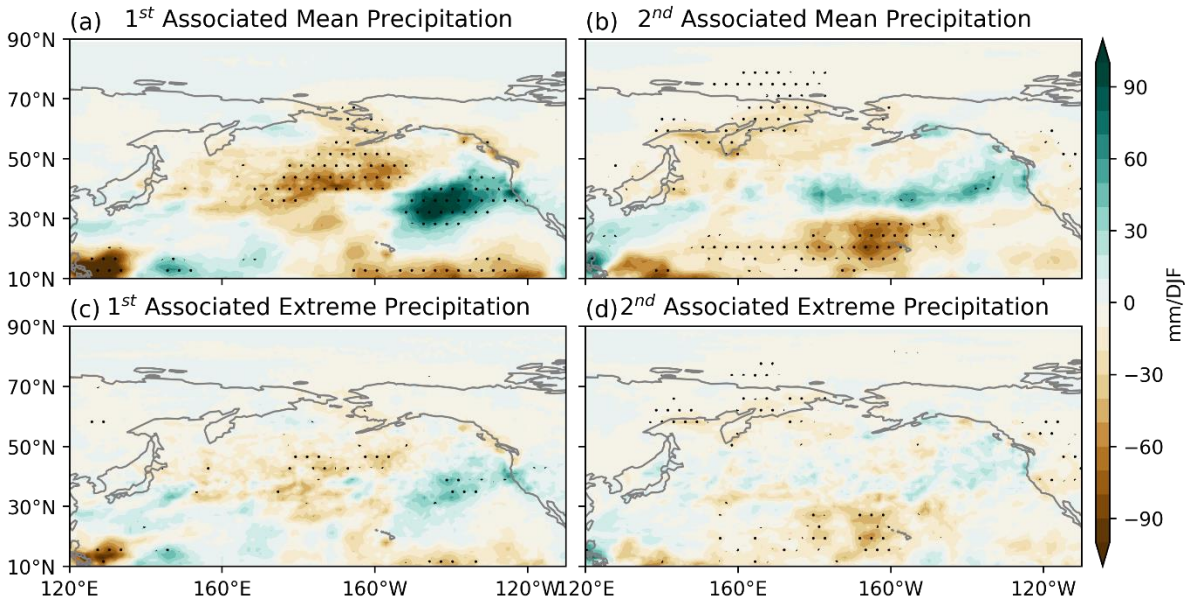

Figure 2. As in Figure 1, but for mean precipitation (a), (b) and extreme precipitation (c), (d) anomalies associated with the first and second EOF modes of winter mean AR anomalies over the

Accepted for publication in *Journal of Climate*. DOI 10.1175/JCLI-D-22-0089.1.

North Pacific, respectively. Precipitation anomaly patterns are obtained by regressing their anomaly fields onto the respective standardized principal components (PCs) (i.e., linear regression between the time series of the precipitation anomaly fields and the time series of the standardized PCs). Stippling indicates regions with anomalies significant at 95% confidence level based on Student's t test.

We next switch to the leading EOF modes of ARs over the Atlantic, with the positive phase indicating enhanced AR frequency over the western Europe. The first mode shows substantial increases in AR frequency around $30^{\circ}N$ stretching from the southeast of the U.S. to the Iberian Peninsula and northwest Africa (Fig. 3a). Reduced AR activities occur over higher latitudes stretching from northeast of the U.S. to the northwest of Europe. Consistent with the first mode of the North Atlantic winter AR variability in Li et al. (2022) (see their Fig. 2a), this pattern indicates the equatorward shift of ARs. Slightly higher than normal AR condition is also found over the Labrador Sea. Moreover, the first AR mode is closely related to the North Atlantic Oscillation (NAO) (Hurrell et al. 2003) or a meridional shift of the Atlantic jet. The associated sea level pressure anomaly pattern shows a negative NAO-like pattern, with a positive anomaly poleward of about $70^{\circ}N$ and a low anomaly over the north Atlantic from $30^{\circ}N$ to $50^{\circ}N$. This low anomaly induces a cyclonic anomaly in the IVT field, causing strong onshore IVT anomalies over the Iberian Peninsula and northwest Africa (Fig. 3c). Consistent with the equatorward shift of ARs, the associated zonal wind anomaly pattern also shows an equatorward shift of the jet with weakening of the winds on the poleward side and strengthening of the winds on the equatorward side of the jet (Fig. 3e). The associated IWV anomalies tend to have the same signs with the AR anomalies: regions with positive (negative) AR anomalies are also regions with positive (negative) IWV anomalies (Fig. 3g).

As shown in Figure 3b, the second mode over the Atlantic shows enhanced AR frequency over the AR maximum region and reduced AR frequency on both sides, indicating the narrowing of the AR peak region rather than the shift by the first mode (Fig. 3a). This mode is also identified as the second mode of SST-forced North Atlantic winter AR variability in Li et al. (2022) (see their Fig. 4a). Compared to the spatial pattern in Li et al. (2022), the anomalies of this mode identified here extend more northeastward. This mode results in heightened AR activities over most of the coastal regions along the western Europe. The associated sea level pressure anomaly pattern shows a dipole structure with a low anomaly located at north Atlantic from $40^{\circ}N$ to $70^{\circ}N$ and a high anomaly from $20^{\circ}N$ to $40^{\circ}N$. This

Accepted for publication in *Journal of Climate*. DOI 10.1175/JCLI-D-22-0089.1.

dipole structure enhances onshore IVT along the Europe west coast and also causes strengthening and eastward extension of the jet (Fig. 3d and 3f).

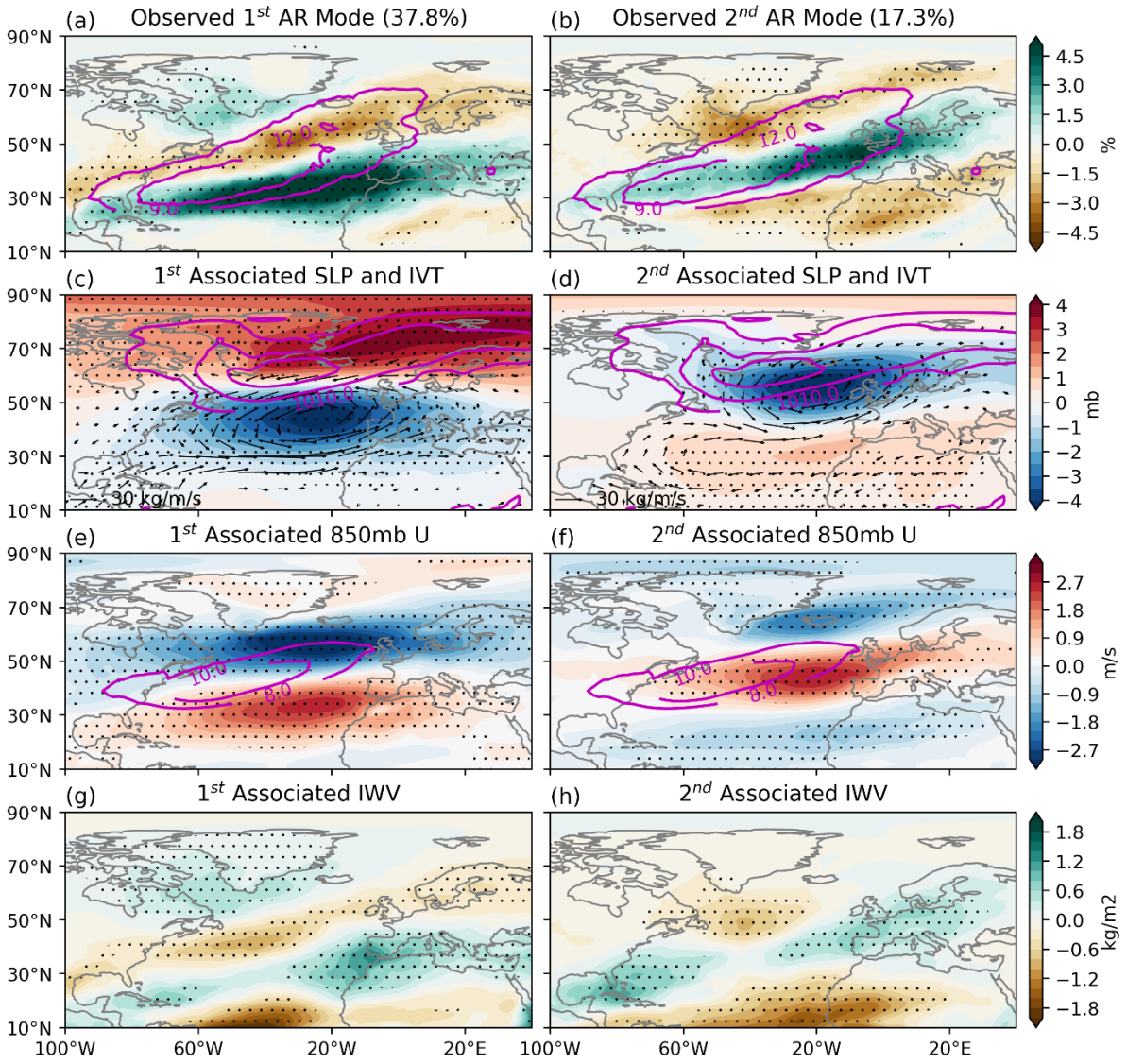

Figure 3. As in Figure 1, but for the North Atlantic: observed AR frequency anomalies (a), (b), sea level pressure and IVT anomalies (c), (d), 850 mb zonal wind anomalies (e), (f), IWV anomalies (g), (h) associated with the first and second EOF modes of winter AR anomalies, respectively. Patterns are obtained by regressing their anomaly fields onto the respective standardized principal components (PCs). Solid contours in (a), (b), (c), (d), (e) and (f) indicate the climatology. Shaded contours show the anomalies. Stippling indicates regions with anomalies significant at 95% confidence level based on Student's t test.

Accepted for publication in *Journal of Climate*. DOI 10.1175/JCLI-D-22-0089.1.

The two AR modes over the Atlantic also result in different regional impacts on precipitation. The first mode over the Atlantic is associated with widespread declines in precipitation over the North Atlantic, including large areas along the west coast of Europe and eastern Greenland. Significant decreases in extreme precipitation are only found over the high latitude regions of North Atlantic at around $70^{\circ}N$. But significant increases in precipitation are found over regions at around $30^{\circ}N$, especially over Iberian Peninsula (Fig. 4a). The Iberian Peninsula also tends to experience higher than normal extreme precipitation (Fig. 4c). Consistent with its AR anomaly pattern (Fig. 3b), the second mode tends to enhance both the mean and extreme precipitation over the Iberian Peninsula and Britain (Fig. 4b and 4d). Again, the results shown here are consistent with those based on the precipitation data from ERA-Interim (Fig. S3).

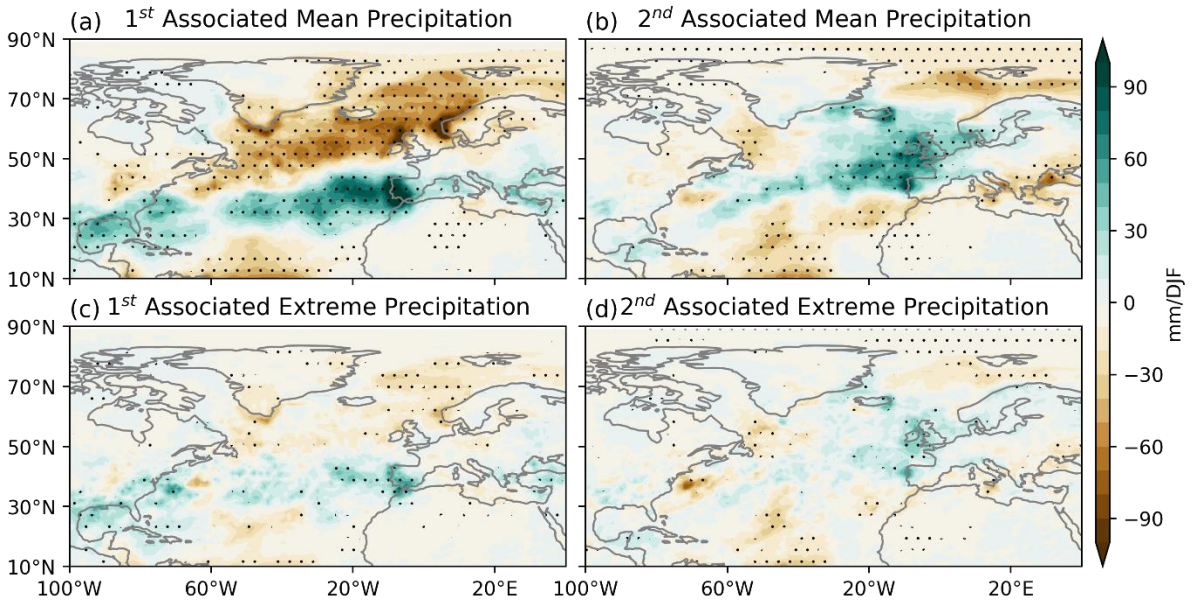

Figure 4. As in Figure 3, but for mean precipitation (a), (b) and extreme precipitation (c), (d) anomalies associated with the first and second EOF modes of winter AR anomalies over the North Atlantic, respectively. Patterns are obtained by regressing their anomaly fields onto the respective standardized principal components (PCs). Stippling indicates regions with anomalies significant at 95% confidence level based on Student's t test.

b. AMIP model evaluation

Before using the AMIP models to quantify the contributions of SST/sea ice forcing versus internal atmospheric variability to the interannual variability of the leading modes in AR

Accepted for publication in *Journal of Climate*. DOI 10.1175/JCLI-D-22-0089.1.

variability, we first evaluate their skills on simulating these modes shown in Figure 1 and 3. Figure 5a and 5b show the winter AR frequency climatology and AR variability defined as the standard deviation of winter AR frequency in observation and simulations, respectively. Overall, AMIP models can reproduce the climatology of AR distribution very well. They capture both the pattern and magnitude of the AR frequency over both the Atlantic and Pacific, except that the AR frequency over the AR maximum region in the Pacific is slightly underestimated. In terms of interannual variability, AMIP models reproduce both the spatial distribution and magnitude of the variability with high fidelity. They capture the maximum variability on the equatorward side of the climatological AR peak region. Decomposition of the AR variability in models shows that both the boundary-forced variability and the internally driven variability maximize over the equatorward side of the AR peak region (Fig. 5c and 5d), and that internally driven variability dominates over the boundary-forced variability at nearly all grid points. We also note that, for the leading AR modes, the percentage of variability explained by the boundary forcing can be greater than that for each grid point, which will be elaborated in section 4.

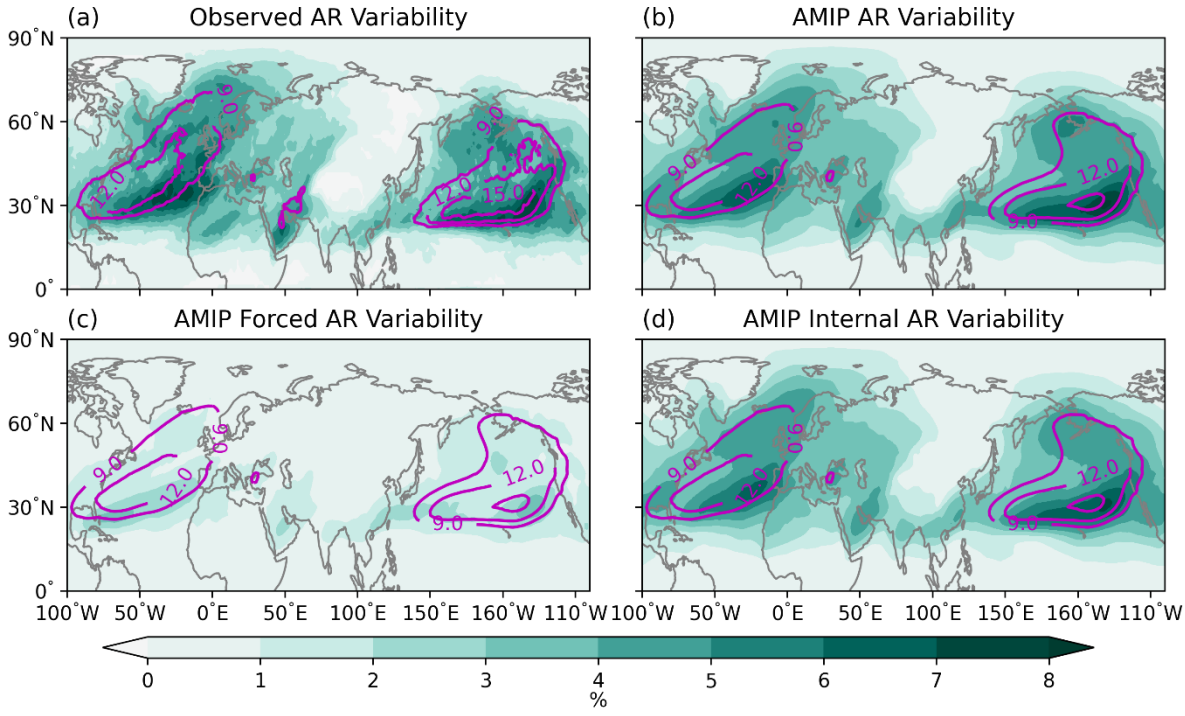

Figure 5. Observed (a) and simulated ensemble mean (b) AR climatology (solid contours) and variability (shaded contours). AR variability is defined as the standard deviation of the winter mean AR frequency. (c) and (d) show the forced and the internally driven components of the total

Accepted for publication in *Journal of Climate*. DOI 10.1175/JCLI-D-22-0089.1.

variability in the AMIP models for each grid point. Forced variability is calculated as the standard deviation of the ensemble mean winter AR frequency across the 35 winters. Internally driven variability is estimated by the multi-year average of the standard deviations across all model anomalies relative to the ensemble mean (i.e. after removing the forced component).

We next extract the leading modes of AR variability in the AMIP models using EOF analysis and evaluate how well models simulate the spatial structure of the observed leading modes using centered pattern correlation. Centered pattern correlation is the grid-by-grid spatial correlation between two anomaly spatial maps. The anomalies are computed by removing their own spatial mean from each map (centered). It measures the similarity of the spatial patterns between two maps. When performing EOF analysis on observations and simulations to extract the leading modes of the same field, the order of the leading modes in a model may not match those in observations. To resolve this problem, we apply the EOF swapping method (Lee et al. 2021, 2019). For each ocean basin, we retain the first 3 leading modes identified in a model and calculate the pattern correlations between the first mode in observation and each of the 3 leading modes in the model. The mode in a model which has the highest correlation with the observed mode is then identified as the matching mode. Similarly, to identify the corresponding second mode in a model, the pattern correlations between the observed second mode and each of the remaining 2 modes in the model are calculated. The simulated mode with the highest pattern correlation is identified as the second mode.

Figure 6 shows that AMIP models generally have high skills in reproducing the spatial structure of the observed modes, with the ensemble mean pattern correlations being 0.85, 0.69, 0.85 and 0.75 for the first and second modes in the Pacific and Atlantic, respectively. Models tend to simulate the first mode of each basin better compared to the second mode. Also, the box and whisker plots on the right show that the distribution for the 30-member ensemble, with one member from each of 30 AMIP models, is similar to that of the 40-member ensemble, with ten members from each of 4 AMIP models. This suggests that inter-member spread within one model is comparable to the inter-model spread, indicating that internal atmospheric variability is an important factor in causing the spread in skills, and that individual model biases play a less important role.

Accepted for publication in *Journal of Climate*. DOI 10.1175/JCLI-D-22-0089.1.

Moreover, the analysis on observation in section 3a has suggested that there is a tight relationship between the AR variability and circulation variability on the interannual timescale. That is, the PCs of the EOF modes derived from AR variability are strongly correlated with the corresponding PCs of the EOF modes derived from 850 mb zonal wind variability. Figure 7 shows that models are able to simulate this tight interannual relationship between AR variability and wind variability. The ensemble mean correlations for the PCs of the corresponding first and second AR/wind modes over the Pacific and Atlantic are 0.80, 0.69, 0.84 and 0.72, respectively. The observed correlations generally fall within the 25th-75th percentile range of the inter-model spread, except for the second mode in the Atlantic which falls at the high end of the model spread.

In summary, the above results on the model evaluation suggest that AMIP models are capable of simulating the observed winter AR variability over the Northern hemisphere with high skills, justifying their uses to further investigate the roles of SST/sea ice forcing versus internal atmospheric variability in driving the observed AR variability.

Accepted for publication in *Journal of Climate*. DOI 10.1175/JCLI-D-22-0089.1.

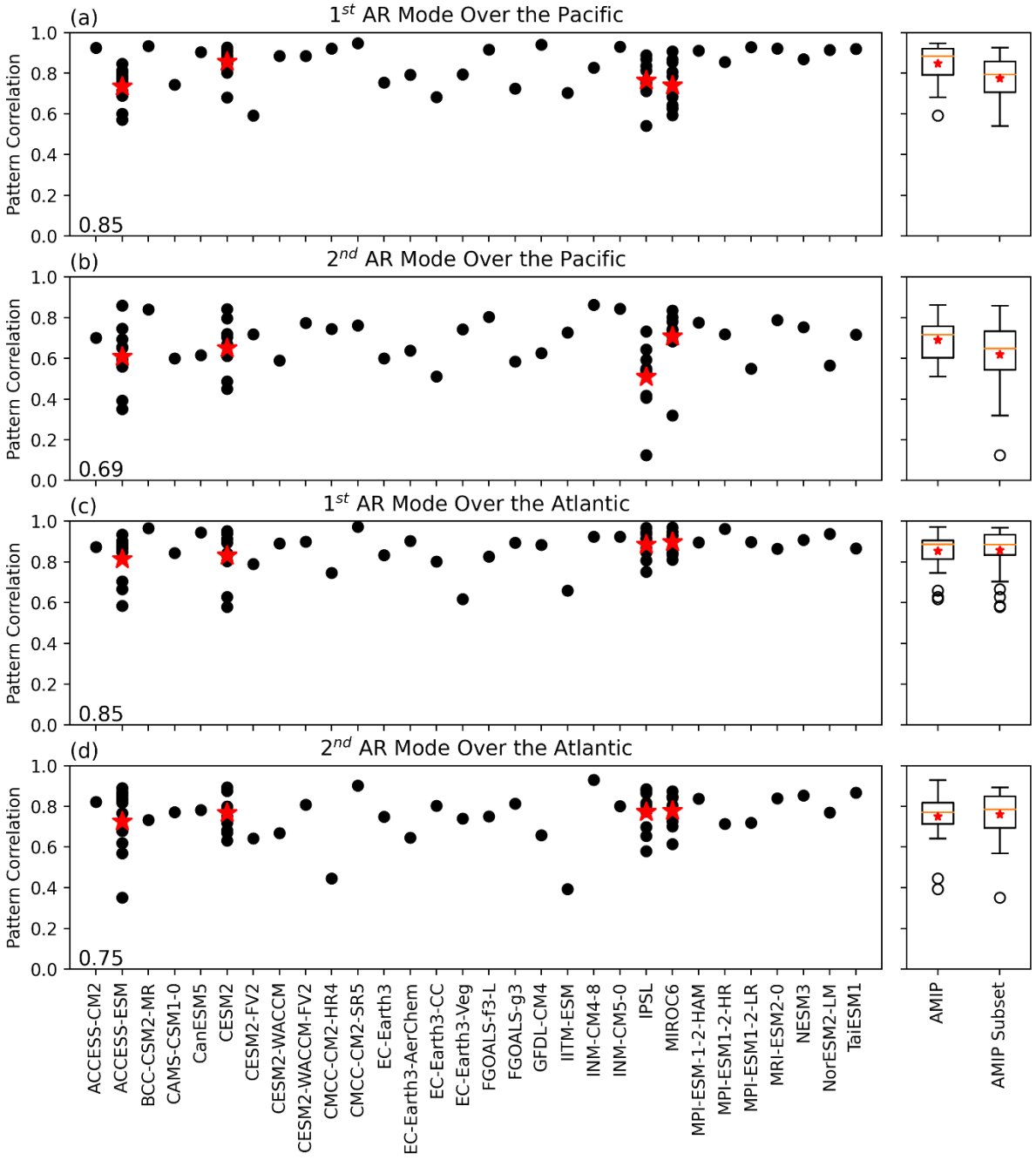

Figure 6. Centered pattern correlations between observation and simulations of the AR anomalies associated with the first (a), (c) and second (b), (d) EOF modes of AR variability over the North Pacific and North Atlantic, respectively. Values at the lower left corner indicate the ensemble mean pattern correlations. Four of the models (ACCESS-ESM, CESM2, IPSL and MIROC6) have ten members. Their ensemble means are indicated by a red star. The box and whisker plots on the right show the inter-model spreads of the pattern correlations for the 30-member AMIP ensemble with only the first member of each model ("AMIP") and the 40-member ensemble from the four models which each has 10 members ("AMIP Subset"). The box shows the 25th and 75th percentile of the spread. The upper and lower whiskers are defined by the formula $75^{th}\ percentile + 1.5 \times (75^{th}\ percentile -$

Accepted for publication in *Journal of Climate*. DOI 10.1175/JCLI-D-22-0089.1.

$25^{th}\ percentile$) and $25^{th}\ percentile - 1.5\ \times (75^{th}\ percentile - \ 25^{th}\ percentile)$, respectively. Values outside of the whiskers are considered as outliers. The orange horizontal lines show the median while the red stars ensemble means.

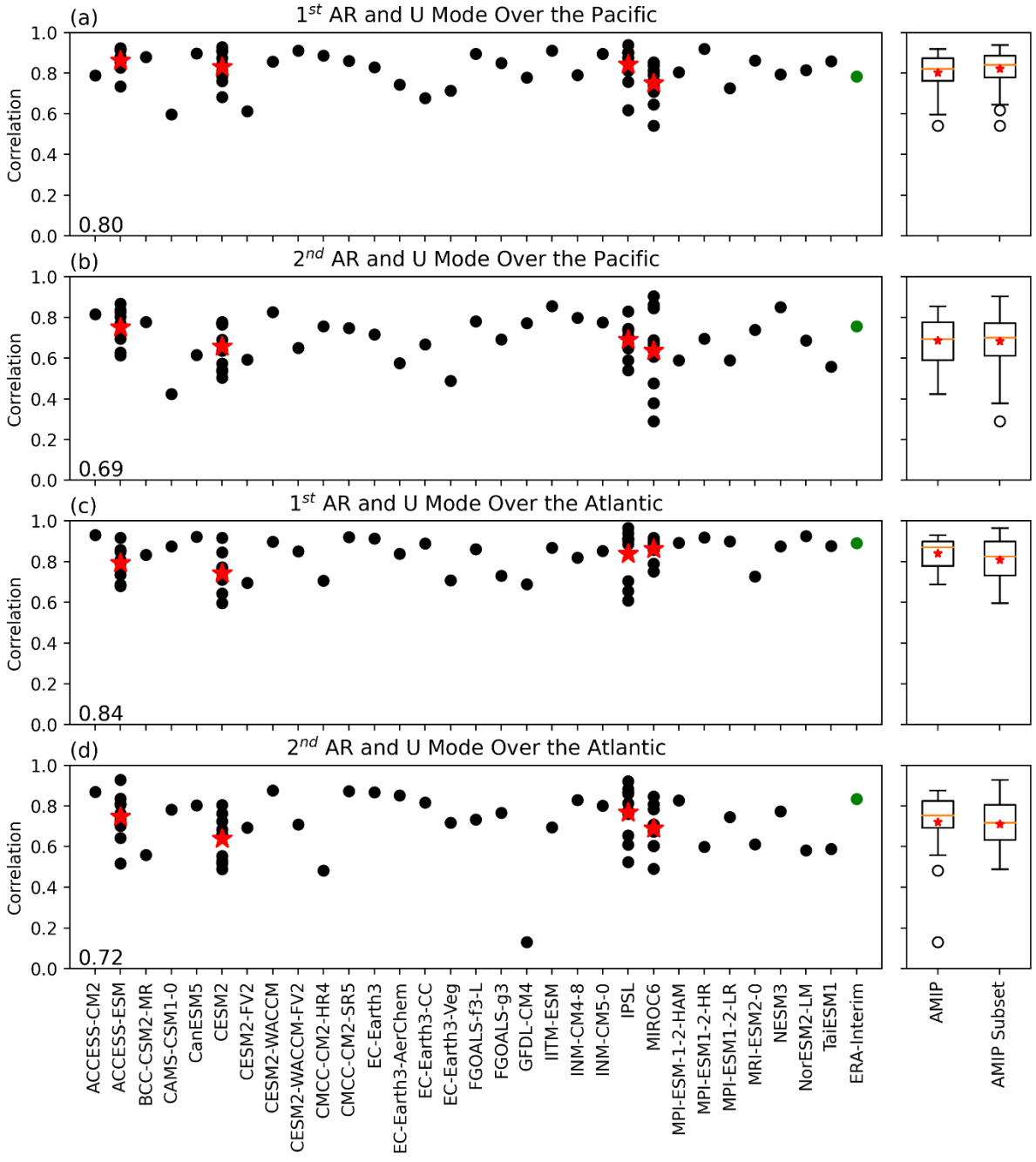

Accepted for publication in *Journal of Climate*. DOI 10.1175/JCLI-D-22-0089.1.

Figure 7. As in Fig. 6, for correlations between the principal components (PCs) associated with the EOF modes of AR anomalies and the corresponding PCs associated with EOF modes of 850 mb zonal wind anomalies for the first (a), (c) and second (b), (d) modes over the North Pacific and North Atlantic, respectively. Values at the lower left corner indicate the ensemble mean correlations. Four of the models (ACCESS-ESM, CESM2, IPSL and MIROC6) have ten members. Their ensemble means are indicated by a red star. Green dots represent the observed values. The box and whisker plots on the right show the inter-model spreads of the correlations for the 30-member AMIP ensemble ("AMIP") and the 40-member ensemble from the four models which each has 10 members ("AMIP Subset"). The box shows the 25th and 75th percentile of the spread. The upper and lower whiskers are defined by the formula $75^{th}\ percentile + 1.5\ \times (75^{th}\ percentile -\ 25^{th}\ percentile)$ and $25^{th}\ percentile - 1.5\ \times (75^{th}\ percentile -\ 25^{th}\ percentile)$, respectively. Values outside of the whiskers are considered as outliers. The orange horizontal lines show the median while the red stars ensemble means.

4. Internal atmospheric variability versus SST/sea ice forced variability

a. SVD modes of ARs and associated SST patterns

Having evaluated the EOF modes of individual models with the observed EOF modes, we next extract the SVD modes of ARs based on the interannual covariance between observation and models. This SVD analysis yields a pair of spatial patterns with the largest squared temporal covariances between observation and models. The SVD patterns for observation with the largest squared covariances resemble the observed EOF patterns that explain the largest percentages of AR variance (Figs. 1, 3 and 8), and the SVD patterns for models provide estimates for all the AMIP models.

Figure 8 shows that the SVD patterns of the AMIP models successfully reproduce the spatial structures in observation over both the Atlantic and Pacific, although there are minor differences between observation and simulations for the first mode over the Pacific and the second mode over the Atlantic. Specifically, for the first mode in the Pacific, models are able to capture the negative anomalies over the central north Pacific north of $30^{\circ}N$. They also produce a band of strong positive anomalies at the AR peak region. However, the positive anomalies in the ERA-Interim are tilted more northeastward and impinging toward the northwest US, while the positive anomalies in the AMIP models are more zonally oriented, making California as the regions mostly affected by this mode. For the second mode over the Atlantic, despite models being able to reproduce the tri-pole pattern with positive anomalies

Accepted for publication in *Journal of Climate*. DOI 10.1175/JCLI-D-22-0089.1.

at the AR peak region and negative anomalies on both sides, the positive anomalies in the models shift southwestward compared to observation.

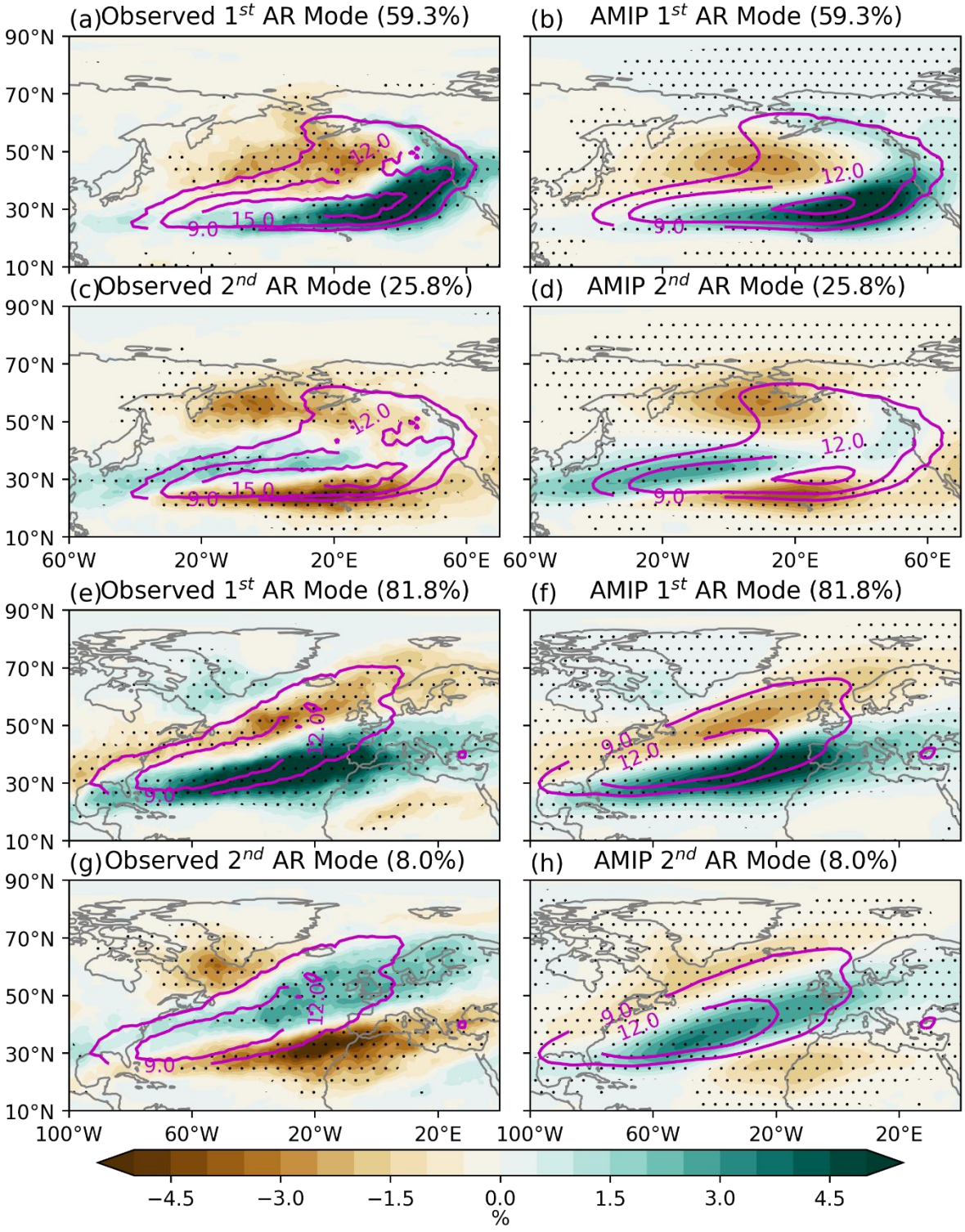

Accepted for publication in *Journal of Climate*. DOI 10.1175/JCLI-D-22-0089.1.

Figure 8. Leading modes of AR anomalies obtained from the SVD analysis of the covariance between observation and simulations. First (a), (b) and second (c), (d) modes of AR anomalies over the North Pacific. First (e), (f) and second (g), (h) modes of AR anomalies over the North Atlantic. Left and right panels display results from observation and simulations, respectively. The values in the title of each subpanel indicate the percentage of squared covariance explained by each SVD. Anomaly patterns in observation are obtained by regressing AR anomalies onto the standardized expansion coefficients (ECs) of 35 winters. Regressions in simulations are based on the 1050 winters across all ensemble members (30 members, each has 35 winters). Solid contours indicate climatology of winter AR frequency. Shaded contours represent anomalies. Stippling indicates regions with anomalies significant at the 95% confidence level based on Student's t test.

The SST anomaly patterns corresponding to these leading SVD modes are displayed in Figure 9 by regressing the SST anomalies onto the standardized ECs of the observation and the ensemble mean EC of the AMIP models for the 35 winters. Over the Pacific, the first mode of AR variability is associated with an SST pattern which resembles the positive phase of ENSO (Fig. 9a and 9b). Indeed, the observed nino3.4 index is strongly correlated with the ensemble mean EC of the AMIP models at 0.76. Widespread of warm anomalies extend from the eastern equatorial Pacific and reach the western equatorial Pacific. The warm anomalies spread toward the extratropics along the eastern Pacific and reach the north Pacific above $40^{\circ}N$. Encircled by the positive anomalies, negative SST anomalies originated from western equatorial Pacific extend northeastward and southeastward in the Northern and Southern Hemispheres, respectively. Significant positive SST anomalies are also found in the Indian Ocean. Moreover, the SST anomalies associated with the second AR mode also show positive anomalies over the equatorial eastern Pacific (Fig. 9c and 9d). However, compared to the pattern associated with the first mode, the positive anomalies are more confined zonally in observation (Fig. 9c), and both zonally and meridionally in models (Fig. 9d). The negative anomalies originating from the equatorial western Pacific extend more eastward and northward. This SST anomaly pattern over the Pacific bears strong resemblance to the North Pacific Mode (NPM) (Deser and Blackmon 1995; Park et al. 2012). Widespread positive anomalies are also found over the Indian Ocean and western Pacific along the East Asian coast. Further analysis shows that the SST patterns over the Pacific associated with the first and second modes of AR variability also resemble the first and second leading EOF modes of the observed interannual SST variability over the North Pacific (Fig. S4).

Accepted for publication in *Journal of Climate*. DOI 10.1175/JCLI-D-22-0089.1.

For the Atlantic AR modes (Fig. 9e, f, g, and h), the associated SST anomaly patterns over the Pacific are very similar to those associated with the AR modes of the Pacific, but with slightly smaller magnitude and shrinked areas with significant anomalies. Stronger and significant SST anomalies are found over the Atlantic, highlighting an important role that Atlantic SST plays in modulating the AR variability locally.

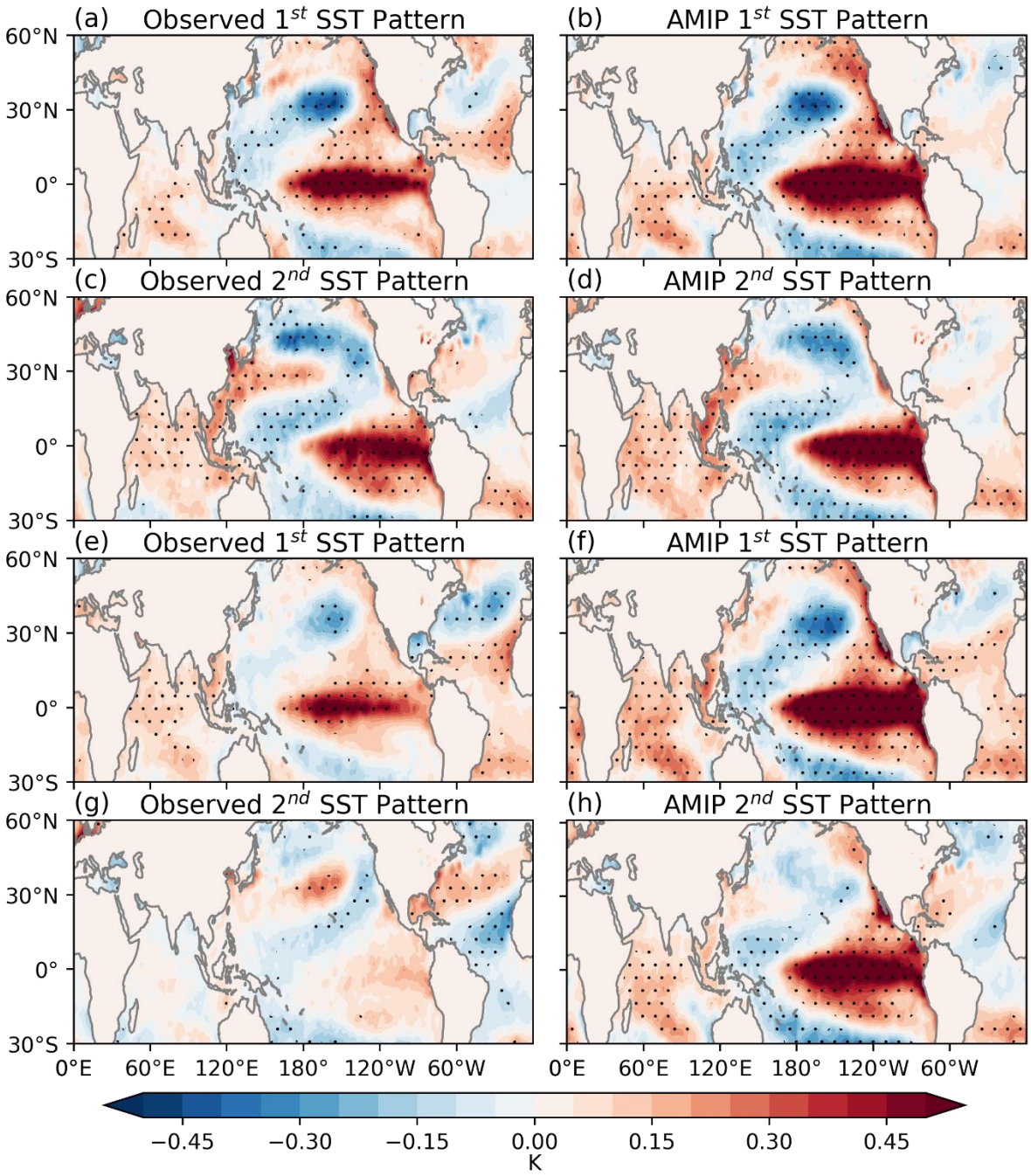

Accepted for publication in *Journal of Climate*. DOI 10.1175/JCLI-D-22-0089.1.

Figure 9. As in Fig. 8, but for SST anomalies associated with the leading modes of AR anomalies obtained from the SVD analysis of the covariance between observation and simulations. First (a), (b) and second (c), (d) modes of SST anomalies over the North Pacific. First (e), (f) and second (g), (h) modes of SST anomalies over the North Atlantic. Left and right panels show results from observation and simulations, respectively. Anomaly patterns in observation are obtained by regressing the SST anomalies onto the expansion coefficients (ECs) of the 35 winters. Anomalies in simulations are based on the ensemble mean EC. Stippling indicates regions with anomalies significant at the 95% confidence level based on Student's t test.

The results in Figure 9 also indicate that the SST patterns in observation tend to be less coherent and significant compared to the SST patterns obtained from simulations, and the differences are especially pronounced for the Atlantic modes (Fig. 9e and 9g). Since the SST patterns from simulations are obtained by regressing the SST anomalies onto the ensemble mean EC, these SST patterns are thus associated mostly with the forced AR variability. Therefore, the differences between SST patterns in observation and simulations imply a large fraction of internally driven variability contained in the observed ECs, especially for the modes in the Atlantic.

b. Relative roles of SST/sea ice forcing versus internal atmospheric variability in driving AR variability

We next quantify the roles of SST/sea ice forcing versus internal atmospheric variability in the leading modes of AR interannual variability using the coefficient of the determination (r^2) approach (Figure 10). Indeed, internal atmospheric variability plays an important role in driving the AR variability over both the Pacific and Atlantic as indicated by the large inter-model spread in the ECs. Over the Pacific, about half of the variance in the leading modes can be explained by the SST forced variability, but that fraction drops to about a quarter for the Atlantic modes, confirming that internal atmospheric variability indeed plays a more important role in driving the AR variability over the Atlantic.

Given such an important role internal atmospheric variability plays in the AR variability, can it alone drive the formation of the leading AR modes shown in Figure 8? To answer this question, we apply EOF analysis to the intra-ensemble AR anomalies based on model simulations. To obtain the intra-ensemble AR anomalies, for each model, we first removed their own winter AR frequency climatology from the winter AR frequency time series. After that, the ensemble mean anomalous winter AR frequency was calculated which represents the

Accepted for publication in *Journal of Climate*. DOI 10.1175/JCLI-D-22-0089.1.

forced AR variability. This forced component was then removed from the anomalous winter AR frequency of each model to get the internally driven component. Finally, we concatenated the internally driven components from all models together to obtain the intra-ensemble AR anomalies. Results from this analysis identify leading modes nearly identical to those based on the SVD analysis of the covariance between observation and models or the EOF of individual models or observation (compared Figures 1, 3, 8 and S5), suggesting that the leading modes forced by SST can also occur naturally due to internal atmospheric variability. These results are also consistent with Ma et al. (2021) in which they discover similar leading modes of AR variability by using an ensemble of models driven by the climatological annual cycle of SST from the Polar Amplification Model Intercomparison Project (PAMIP).

Given that both SST/sea ice forcing and internal atmospheric variability play such important roles in shaping the AR variability, their contributions to the magnitude of the total variance are further quantified. We estimate the total variance by calculating the variance of the ECs corresponding to the leading SVD modes during the 35 winters. The total variance of each mode in models is based on ECs across all models. Figure 11 indicates that AMIP models underestimate the variance for all modes, with the largest underestimate for the second Atlantic mode. We further estimate the magnitude of the forced variance in models by calculating the variance of the ensemble mean EC of each mode. The forced variance accounts for about half of the total variance for the Pacific modes, while that number drops to about 40% and 30% for the first and second Atlantic modes, respectively. These results further support that AR variability over the Atlantic is more strongly modulated by internal atmospheric variability compared to the Pacific AR variability.

Lastly, we investigate how much of the total observed variability in the AR EOF modes is regulated by the leading EOF modes of SST over each of the ocean basins by using the coefficient of determination (r^2) approach. The first SST mode over the Pacific associated with ENSO significantly correlates with both the first modes of the Pacific and Atlantic and explains about 30% and 17% of their observed total variance, respectively. The second SST mode over the Pacific, which resembles the NPM, exerts strong influences on the second Pacific AR mode, and explains about half of the observed total variance of this mode. Moreover, we perform EOF analysis on the SST anomalies over the North Atlantic (Figure S6). The first mode shows a tri-pole pattern of SST anomalies over the North Atlantic, which resembles the SST anomaly pattern of the second AR mode over the Atlantic. Similar to the

Accepted for publication in *Journal of Climate*. DOI 10.1175/JCLI-D-22-0089.1.

SST anomaly pattern of the first AR mode over the North Atlantic, the second mode in SST also shows a dipole pattern over the North Atlantic. Consequently, the leading modes of AR variability over the North Atlantic are also related to the leading SST modes over the North Atlantic. The first and second SST modes in the Atlantic explains about 20% of the observed total variance of the second and first modes of AR variability, respectively.

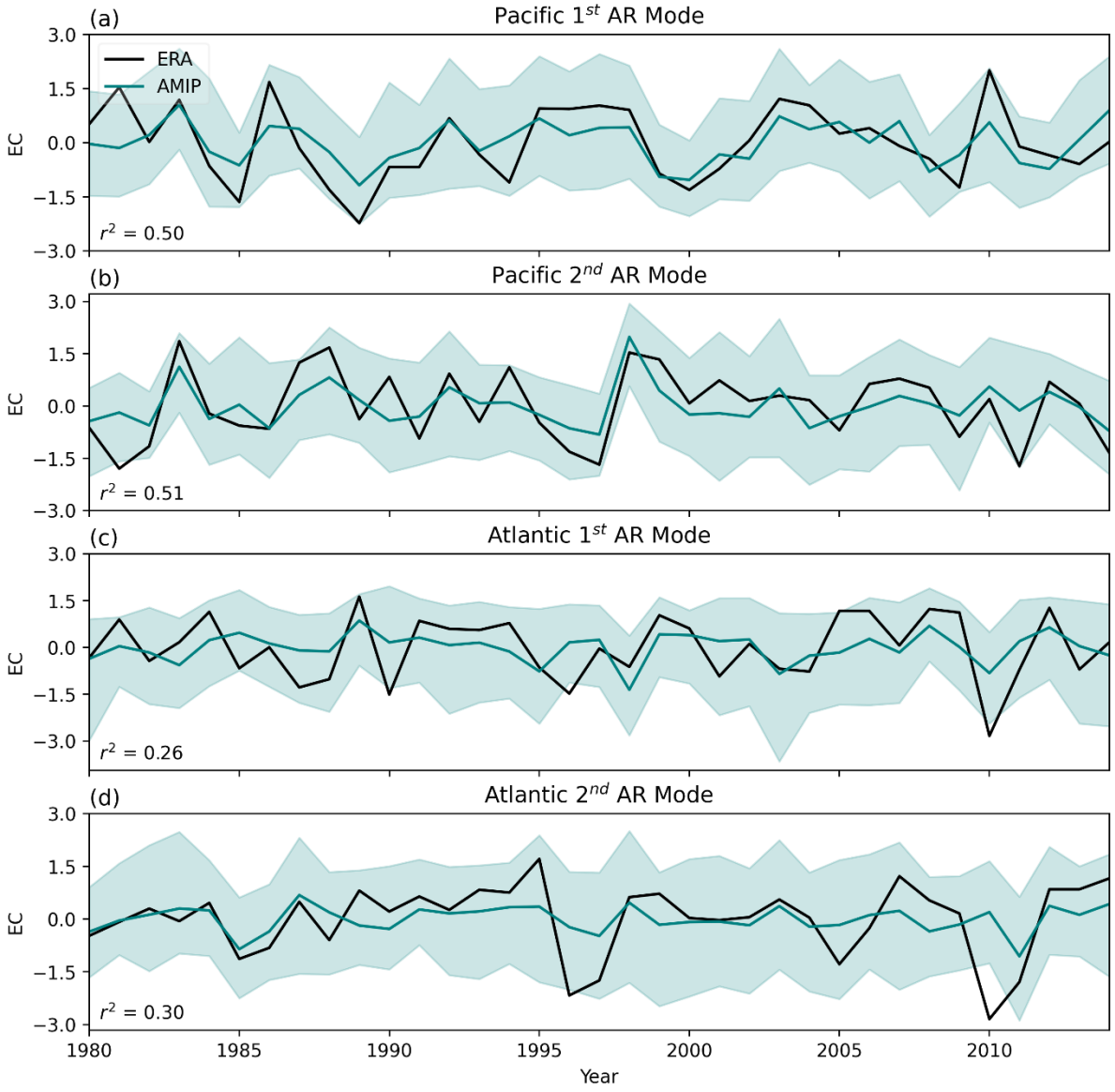

Figure 10. Expansion coefficients (ECs) for the first (a), (c) and second (b), (d) SVD modes of AR anomalies over the North Pacific and North Atlantic, respectively. Black and teal curves show ECs for the observation and ensemble mean EC for simulations, respectively. R^2 between the

Accepted for publication in *Journal of Climate*. DOI 10.1175/JCLI-D-22-0089.1.

observed ECs and the corresponding simulated ensemble mean EC are shown at the lower left corners of each panel. The shading shows the 2.5th and 97.5th percentile range of the model spread.

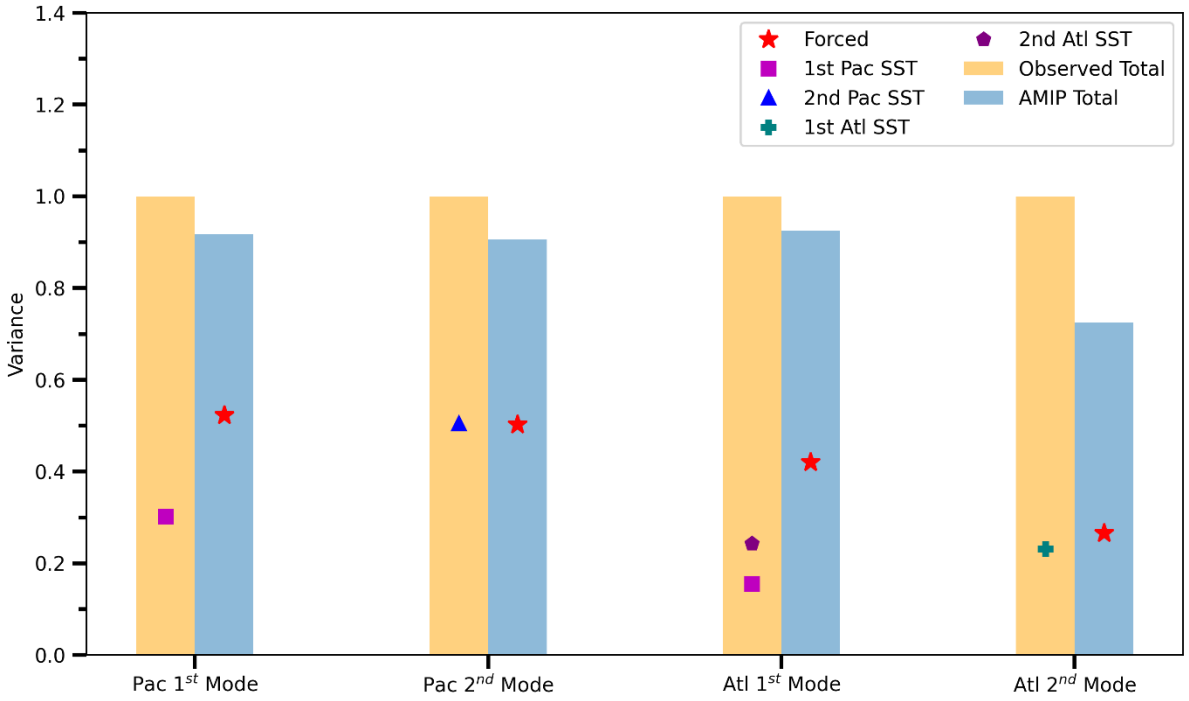

Figure 11. Magnitude of the total variance (yellow bars) in observation and simulations (blue bars). Red stars indicate the magnitude of the forced variance. Markers indicate the contributions of different SST modes to the total variance of the observed leading SVD modes of AR anomalies. The values for each mode are scaled by the observed total variance. See the text for more information on how the statistics shown in this figure are calculated.

c. Tropical versus extratropical SST in driving the forced AR variability

Based on the SST patterns associated with the leading modes of AR variability (Figure 9), significant SST anomalies can be seen over both the tropical and extratropical oceans, suggesting both play roles in driving the forced AR variability. To better understand the relative roles of tropical SST versus extratropical SST in driving the forced AR variability, we analyze two additional ensembles based on CESM1. One ensemble with 10 members, termed "GOGA", is driven by observed SST globally. Another ensemble also with 10 members, termed "TOGA", is driven by observed SST only in the tropics. Despite their smaller ensemble size compared to the 30-member AMIP ensemble, they are still useful in providing an estimate on the relative roles of tropical SST versus extratropical SST in AR

Accepted for publication in *Journal of Climate*. DOI 10.1175/JCLI-D-22-0089.1.

variability. The same combined SVD analysis is applied to the covariance matrix between observation and simulations based on GOGA.

Results show that GOGA is able to reproduce both the leading SVD modes of AR variability over the Pacific and the first mode over the Atlantic. The strengthening and eastward extension of ARs associated with the second mode over the Atlantic are too weak in the models (Fig. S7). Compared to the results based on the AMIP ensemble, the 10-member GOGA underestimates the fraction of forced variance in the first Pacific mode while overestimating that in the second Atlantic mode (Fig. 12). The fraction of forced variance for the second Pacific mode and first Atlantic mode are consistent with those based on the AMIP ensemble. They explain about half and a quarter of the total variance, respectively, for the second Pacific mode and the first Atlantic mode. Consistent with the results based on the AMIP ensemble, AR variability in the Pacific is more strongly controlled by the SST variability compared to the AR variability in the Atlantic. For the forced variability, the role of the tropical SST variability dominates over the extratropical SST variability for both the leading modes over the Pacific, explaining about 77% and 71% of the total forced variability, respectively. Over the Atlantic, tropical SST explains about 49% and 56% of the total forced variability for the first and second mode, respectively, suggesting comparable role tropical SST versus extratropical SST plays in driving these modes.

Accepted for publication in *Journal of Climate*. DOI 10.1175/JCLI-D-22-0089.1.

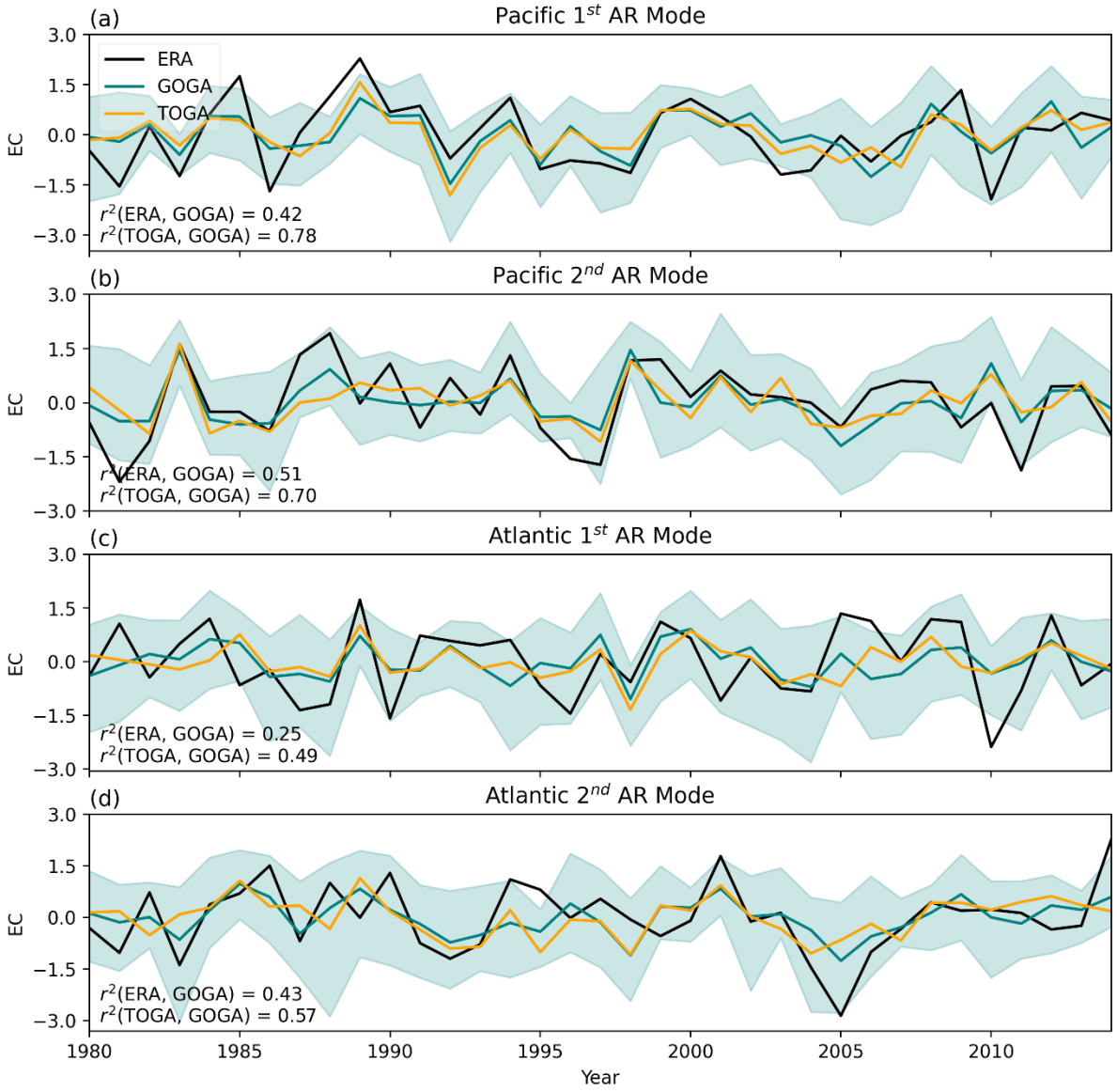

Figure 12. Same as Figure 10, but for the results based on the GOGA and TOGA ensembles.

5. Conclusions

A better understanding of the mechanisms controlling the interannual AR variability is crucial for water resource management and hazard warning (Paltan et al. 2017; Henn et al. 2020; Dettinger et al. 2011; Ralph et al. 2006). In this study, we identify and characterize the leading modes of AR variability over both the Pacific and Atlantic during boreal winter, with distinct precipitation patterns and impacts over different coastal regions, similar to Dong et al. (2018) and Li et al. (2022). Over the Pacific, the first mode is characterized by a dipole structure with substantial enhanced AR frequency over the AR peak region and reduced AR activities further north (Fig. 1a). The second mode depicts a tri-pole pattern with a band of

Accepted for publication in *Journal of Climate*. DOI 10.1175/JCLI-D-22-0089.1.

positive anomalies extended from west Pacific at about $30^{\circ}N$ to northeast Pacific, accompanied by negative anomalies on both sides (Fig. 1b). The first AR mode in the Pacific significantly modulates precipitation along the U.S. west coast while the second mode mostly affects precipitation over the U.S. Northwest and British Columbia (Fig. 2). Over the Atlantic, the first mode represents the equatorward shift of the ARs, with significant impacts along the entire west coast of Europe, while the second mode represents strengthening and eastward extension of the AR peak region, with the effects confined more toward the southern part of the west coast (Fig. 3a and 3b). It is worth mentioning that, given the strong correlation between the leading modes of AR variability and the corresponding leading modes of 850 mb zonal wind variability, the spatial patterns of the leading AR modes identified in this study do not depend on the AR detection algorithms used. Indeed, these leading modes of AR variability can also be identified in nearly all of the Tier 1 AR catalogues based on the global AR detection algorithms participated in the Atmospheric River Tracking Method Intercomparison Project (not shown; Shields et al. 2018). As such, the AR modes identified here can serve as metrics to evaluate the AR variability in climate models.

We have quantified, perhaps for the first time, the relative roles of SST forcing versus internal atmospheric variability in driving the interannual variability of the leading AR modes by using a large ensemble of AMIP-type models participated in the CMIP6. We first show that the AMIP models have high skills in simulating many aspects of these modes, including their spatial structure and the strong coupling between circulation variability and AR variability.

Then, a combined SVD analysis using both observation and AMIP models is adopted to extract the leading modes of AR co-variability between observation and models. Based on the SVD analysis, the forced variability explains about half of and a quarter of the total variance for the leading AR modes over the Pacific and the Atlantic, respectively. These results suggest higher predictability of the AR variability over the Pacific compared to the Atlantic. The associated SST patterns for the leading modes over the Pacific bear marked resemblance to the corresponding leading modes of North Pacific SST, characterized by an ENSO-like (Xiong and Ren 2021; Kim et al. 2017) and an NPM-like (Deser and Blackmon 1995; Park et al. 2012) anomalous SST pattern, respectively. Further analysis reveals that these two Pacific SST modes also play some roles in the corresponding leading modes of

Accepted for publication in *Journal of Climate*. DOI 10.1175/JCLI-D-22-0089.1.

Atlantic AR variability. Additionally, a model ensemble driven by observed SST only in the tropical oceans is used to quantify the relative importance of tropical versus extratropical SST in exciting these leading modes of AR variability. Results show that tropical SST variability dominates over extratropical SST variability and contributes more to the total forced AR variability over the Pacific. Over the Atlantic, the tropical and extratropical SST play comparable roles in the formations of the leading modes of AR variability.

Our findings may have important implications for the interannual variations of boreal winter precipitation. While the SST variability modes, such as ENSO or NPM, provide some sources of predictability for the North American west coast, the predictability is limited by the internal variability of the atmosphere (Teng and Branstator 2017; Zhang et al. 2018; Dong et al. 2018; Kumar and Chen 2017; Chen and Kumar 2018; Deser et al. 2018; Cash and Burls 2019), especially for the well-known failed 2016 winter rains in Southern California (Zhang et al. 2018; Patricola et al. 2020). Dong et al. (2018) estimates that about 80% of the interannual variability of winter precipitation in California is controlled by internal atmospheric variability, but we find that internal atmospheric variability only accounts for about half of the variability in the two Pacific AR modes. As both AR modes can influence the North American west coast (Fig. 2), this indicates that the winter precipitation related to the two AR modes may be more predictable. Our analysis also indicates that SST variability over the Pacific basin can influence the AR variability not only locally over the Pacific, but also remotely over the Atlantic (Fig. 9), similar to the remote influence of ENSO on NAO (Li and Lau 2012; Brönnimann 2007; Zhang et al. 2019). Moreover, the leading AR modes forced by SST can appear as the dominant pattern in the AR response to Arctic sea ice loss (Ma et al. 2021) and also occur naturally due to internal atmospheric variability (Fig. S5). Further research is needed to better understand the mechanisms of internal atmospheric variability in driving AR variability at shorter timescales. This can potentially improve AR forecast at S2S timescale. Overall, the results presented in this study not only improve our physical understanding of the AR variability, but may also lead to better seasonal AR prediction over the densely populated regions, such as the North American west coast and the Western Europe.

Acknowledgments.

Accepted for publication in *Journal of Climate*. DOI 10.1175/JCLI-D-22-0089.1.

Weiming Ma and Gang Chen are supported by National Science Foundation Grants AGS-1832842 and NASA Grant 80NSS-C21K1522. We thank three anonymous reviewers for their constructive feedback that greatly improved the manuscript. The authors would like to acknowledge high-performance computing support from Cheyenne (https://doi.org/10.5065/D6RX99HX) provided by NCAR's Computational and Information Systems Laboratory, sponsored by the National Science Foundation.

Data Availability Statement.

Data from the AMIP models participated in CMIP6 can be found on the Earth System Grid: https://esgf-node.llnl.gov/projects/cmip6/. Data from GOGA can be found at: https://www.earthsystemgrid.org/dataset/ucar.cgd.ccsm4.cam5.prescribed_sst_amip.goga.html. Data from TOGA can be found at: https://www.earthsystemgrid.org/dataset/ucar.cgd.ccsm4.cam5.prescribed_sst_amip.toga.html. ERA-Interim is available for download through: https://www.ecmwf.int/en/forecasts/datasets/reanalysis-datasets/era-interim/. The SST dataset can be found at: https://www.metoffice.gov.uk/hadobs/hadisst/. The GPCP dataset can be found at: https://www.ncei.noaa.gov/products/climate-data-records/precipitation-gpcp-daily.

REFERENCES

Baggett, C. F., E. A. Barnes, E. D. Maloney, and B. D. Mundhenk, 2017: Advancing atmospheric river forecasts into subseasonal-to-seasonal time scales. *Geophys. Res. Lett.*, **44**, 7528–7536, https://doi.org/10.1002/2017GL074434.

Barnes, E. A., and L. Polvani, 2013: Response of the midlatitude jets, and of their variability, to increased greenhouse gases in the CMIP5 models. *J. Clim.*, **26**, 7117–7135, https://doi.org/10.1175/JCLI-D-12-00536.1.

Bond, N. A., M. F. Cronin, H. Freeland, and N. Mantua, 2015: Causes and impacts of the 2014 warm anomaly in the NE Pacific. *Geophys. Res. Lett.*, **42**, 3414–3420, https://doi.org/10.1002/2015GL063306.

Bozkurt, D., O. L. Sen, Y. Ezber, B. Guan, M. Viale, and F. Caglar, 2021: Influence of African Atmospheric Rivers on Precipitation and Snowmelt in the Near East's Highlands. *J. Geophys. Res. Atmos.*, **126**, 1–23, https://doi.org/10.1029/2020JD033646.

Accepted for publication in *Journal of Climate*. DOI 10.1175/JCLI-D-22-0089.1.

Bretherton, C. S., C. Smith, and J. M. Wallace, 1992: An Intercomparison of Methods for Finding Coupled Patterns in Climate Data. *J. Clim.*, **5**, 541–560.

Brönnimann, S., 2007: Impact of El Niño-Southern Oscillation on European climate. *Rev. Geophys.*, **45**, https://doi.org/10.1029/2006RG000199.

Cash, B. A., and N. J. Burls, 2019: Predictable and unpredictable aspects of U.S. west coast rainfall and El Niño: Understanding the 2015/16 event. *J. Clim.*, **32**, 2843–2868, https://doi.org/10.1175/JCLI-D-18-0181.1.

Chen, M., and A. Kumar, 2018: Winter 2015/16 atmospheric and precipitation anomalies over North America: El Niño response and the role of noise. *Mon. Weather Rev.*, **146**, 909–927, https://doi.org/10.1175/MWR-D-17-0116.1.

Dee, D. P., and Coauthors, 2011: The ERA-Interim reanalysis: Configuration and performance of the data assimilation system. *Q. J. R. Meteorol. Soc.*, **137**, 553–597, https://doi.org/10.1002/qj.828.

Deser, C., and M. Blackmon, 1995: On the Relationship between Tropical and North Pacific Sea Surface Temperature Variations. *J. Clim.*, **8**, 1677–1680.

——, I. R. Simpson, A. S. Phillips, and K. A. McKinnon, 2018: How well do we know ENSO's climate impacts over North America, and how do we evaluate models accordingly? *J. Clim.*, **31**, 4991–5014, https://doi.org/10.1175/JCLI-D-17-0783.1.

Dettinger, M. D., F. M. Ralph, T. Das, P. J. Neiman, and D. R. Cayan, 2011: Atmospheric rivers, floods and the water resources of California. *Water (Switzerland)*, **3**, 445–478, https://doi.org/10.3390/w3020445.

Dong, L., L. R. Leung, F. Song, and J. Lu, 2018: Roles of SST versus internal atmospheric variability in winter extreme precipitation variability along the U.S. West Coast. *J. Clim.*, **31**, 8039–8058, https://doi.org/10.1175/JCLI-D-18-0062.1.

Eyring, V., S. Bony, G. A. Meehl, C. A. Senior, B. Stevens, R. J. Stouffer, and K. E. Taylor, 2016: Overview of the Coupled Model Intercomparison Project Phase 6 (CMIP6) experimental design and organization. *Geosci. Model Dev.*, **9**, 1937–1958, https://doi.org/10.5194/gmd-9-1937-2016.

Francis, D., K. S. Mattingly, M. Temimi, R. Massom, and P. Heil, 2020: On the crucial role of atmospheric rivers in the two major Weddell Polynya events in 1973 and 2017 in

Accepted for publication in *Journal of Climate*. DOI 10.1175/JCLI-D-22-0089.1.

Antarctica. *Sci. Adv.*, **6**, 1–14, https://doi.org/10.1126/sciadv.abc2695.

Gao, Y., J. Lu, and L. R. Leung, 2016: Uncertainties in projecting future changes in atmospheric rivers and their impacts on heavy precipitation over Europe. *J. Clim.*, **29**, 6711–6726, https://doi.org/10.1175/JCLI-D-16-0088.1.

Gershunov, A., T. Shulgina, F. M. Ralph, D. A. Lavers, and J. J. Rutz, 2017: Assessing the climate-scale variability of atmospheric rivers affecting western North America. *Geophys. Res. Lett.*, **44**, 7900–7908, https://doi.org/10.1002/2017GL074175.

Gorodetskaya, I. V., M. Tsukernik, K. Claes, M. F. Ralph, W. D. Neff, and N. P. M. Van Lipzig, 2014: The role of atmospheric rivers in anomalous snow accumulation in East Antarctica. *Geophys. Res. Lett.*, **41**, 6199–6206, https://doi.org/10.1002/2014GL060881.

Guan, B., and D. E. Waliser, 2015: Detection of atmospheric rivers: Evaluation and application of an algorithm for global studies. *J. Geophys. Res.*, **120**, 12,514-12,535, https://doi.org/10.1002/2015JD024257.

——, D. E. Waliser, N. P. Molotch, E. J. Fetzer, and P. J. Neiman, 2012: Does the Madden-Julian oscillation influence wintertime atmospheric rivers and snowpack in the sierra nevada? *Mon. Weather Rev.*, **140**, 325–342, https://doi.org/10.1175/MWR-D-11-00087.1.

——, D. E. Waliser, F. M. Ralph, E. J. Fetzer, and P. J. Neiman, 2016: Hydrometeorological characteristics of rain-on-snow events associated with atmospheric rivers. *Geophys. Res. Lett.*, **43**, 2964–2973, https://doi.org/10.1002/2016GL067978.

Guirguis, K., A. Gershunov, T. Shulgina, R. E. S. Clemesha, and F. M. Ralph, 2019: Atmospheric rivers impacting Northern California and their modulation by a variable climate. *Clim. Dyn.*, **52**, 6569–6583, https://doi.org/10.1007/s00382-018-4532-5.

Henn, B., K. N. Musselman, L. Lestak, F. M. Ralph, and N. P. Molotch, 2020: Extreme Runoff Generation From Atmospheric River Driven Snowmelt During the 2017 Oroville Dam Spillways Incident. *Geophys. Res. Lett.*, **47**, 1–11, https://doi.org/10.1029/2020GL088189.

Huffman, G. J., R. F. Adler, M. M. Morrissey, D. T. Bolvin, S. Curtis, R. Joyce, B. McGavock, and J. Susskind, 2001: Global precipitation at one-degree daily resolution from multisatellite observations. *J. Hydrometeorol.*, https://doi.org/10.1175/1525-

Accepted for publication in *Journal of Climate*. DOI 10.1175/JCLI-D-22-0089.1.

7541(2001)002<0036:GPAODD>2.0.CO;2.

Hurrell, J. W., Y. Kushnir, G. Ottersen, and M. Visbeck, 2003: An overview of the north atlantic oscillation. *Geophysical Monograph Series*, Vol. 134 of, 1–35.

Kim, H.-M., Y. Zhou, and M. A. Alexander, 2017: Changes in atmospheric rivers and moisture transport over the Northeast Pacific and western North America in response to ENSO diversity. *Clim. Dyn.*, 1–14, https://doi.org/10.1007/s00382-017-3598-9.

Kumar, A., and M. Chen, 2017: What is the variability in US west coast winter precipitation during strong El Niño events? *Clim. Dyn.*, **49**, 2789–2802, https://doi.org/10.1007/s00382-016-3485-9.

Lamjiri, M. A., M. D. Dettinger, F. M. Ralph, and B. Guan, 2017: Hourly storm characteristics along the U.S. West Coast: Role of atmospheric rivers in extreme precipitation. *Geophys. Res. Lett.*, **44**, 7020–7028, https://doi.org/10.1002/2017GL074193.

Lavers, D. A., and G. Villarini, 2013: The nexus between atmospheric rivers and extreme precipitation across Europe. *Geophys. Res. Lett.*, **40**, 3259–3264, https://doi.org/10.1002/grl.50636.

——, and ——, 2015: The contribution of atmospheric rivers to precipitation in Europe and the United States. *J. Hydrol.*, **522**, 382–390, https://doi.org/10.1016/j.jhydrol.2014.12.010.

Lee, J., K. R. Sperber, P. J. Gleckler, C. J. W. Bonfils, and K. E. Taylor, 2019: *Quantifying the agreement between observed and simulated extratropical modes of interannual variability*. Springer Berlin Heidelberg, 4057–4089 pp.

——, ——, ——, K. E. Taylor, and C. J. W. Bonfils, 2021: Benchmarking performance changes in the simulation of extratropical modes of variability across CMIP generations. *J. Clim.*, 1–70, https://doi.org/10.1175/jcli-d-20-0832.1.

Leung, L. R., and Y. Qian, 2009: Atmospheric rivers induced heavy precipitation and flooding in the western U.S. simulated by the WRF regional climate model. *Geophys. Res. Lett.*, **36**, n/a-n/a, https://doi.org/10.1029/2008GL036445.

Li, C., W. Mei, and Y. Kamae, 2022: Variability and predictability of cold-season North Atlantic atmospheric river occurrence frequency in a set of high-resolution atmospheric

Accepted for publication in *Journal of Climate*. DOI 10.1175/JCLI-D-22-0089.1.

simulations. *Clim. Dyn.*, **58**, 2485–2500, https://doi.org/10.1007/s00382-021-06017-y.

Li, Y., and N. C. Lau, 2012: Impact of ENSO on the atmospheric variability over the North Atlantic in late Winter-Role of transient eddies. *J. Clim.*, **25**, 320–342, https://doi.org/10.1175/JCLI-D-11-00037.1.

Ma, W., G. Chen, and B. Guan, 2020a: Poleward Shift of Atmospheric Rivers in the Southern Hemisphere in Recent Decades. *Geophys. Res. Lett.*, submitted, https://doi.org/10.1029/2020GL089934.

——, J. Norris, and G. Chen, 2020b: Projected Changes to Extreme Precipitation Along North American West Coast From the CESM Large Ensemble. *Geophys. Res. Lett.*, **47**, 1–10, https://doi.org/10.1029/2019GL086038.

——, G. Chen, Y. Peings, and N. Alviz, 2021: Atmospheric River Response to Arctic Sea Ice Loss in the Polar Amplification Model Intercomparison Project. *Geophys. Res. Lett.*, 1–12, https://doi.org/10.1029/2021gl094883.

Mattingly, K. S., T. L. Mote, and X. Fettweis, 2018: Atmospheric River Impacts on Greenland Ice Sheet Surface Mass Balance. *J. Geophys. Res. Atmos.*, **123**, 8538–8560, https://doi.org/10.1029/2018JD028714.

McGowan, H., K. Borthwick, A. Schwartz, J. N. Callow, S. Bilish, and S. Browning, 2021: Atmospheric Rivers: An Overlooked Threat to the Marginal Snowpack of the Australian Alps. *J. Hydrometeorol.*, **22**, 2521–2532, https://doi.org/10.1175/jhm-d-20-0293.1.

Mori, M., Y. Kosaka, M. Watanabe, H. Nakamura, and M. Kimoto, 2019: A reconciled estimate of the influence of Arctic sea-ice loss on recent Eurasian cooling. *Nat. Clim. Chang.*, **9**, 123–129, https://doi.org/10.1038/s41558-018-0379-3.

Mundhenk, B. D., E. A. Barnes, E. D. Maloney, and C. F. Baggett, 2018: Skillful empirical subseasonal prediction of landfalling atmospheric river activity using the Madden–Julian oscillation and quasi-biennial oscillation. *npj Clim. Atmos. Sci.*, **1**, 19–21, https://doi.org/10.1038/s41612-017-0008-2.

Nash, D., D. Waliser, B. Guan, H. Ye, and F. M. Ralph, 2018: The Role of Atmospheric Rivers in Extratropical and Polar Hydroclimate. *J. Geophys. Res. Atmos.*, **123**, 6804–6821, https://doi.org/10.1029/2017JD028130.

Paltan, H., D. Waliser, W. H. Lim, B. Guan, D. Yamazaki, R. Pant, and S. Dadson, 2017:

Accepted for publication in *Journal of Climate*. DOI 10.1175/JCLI-D-22-0089.1.

Global Floods and Water Availability Driven by Atmospheric Rivers. *Geophys. Res. Lett.*, **44**, 10,387-10,395, https://doi.org/10.1002/2017GL074882.

Park, J. Y., S. W. Yeh, and J. S. Kug, 2012: Revisited relationship between tropical and North Pacific sea surface temperature variations. *Geophys. Res. Lett.*, **39**, 1–6, https://doi.org/10.1029/2011GL050005.

Patricola, C. M., J. P. O'Brien, M. D. Risser, A. M. Rhoades, T. A. O'Brien, P. A. Ullrich, D. A. Stone, and W. D. Collins, 2020: Maximizing ENSO as a source of western US hydroclimate predictability. *Clim. Dyn.*, **54**, 351–372, https://doi.org/10.1007/s00382-019-05004-8.

Ralph, F. M., P. J. Neiman, G. A. Wick, S. I. Gutman, M. D. Dettinger, D. R. Cayan, and A. B. White, 2006: Flooding on California's Russian River: Role of atmospheric rivers. *Geophys. Res. Lett.*, **33**, L13801, https://doi.org/10.1029/2006GL026689.

Rayner, N. A., D. E. Parker, E. B. Horton, C. K. Folland, L. V. Alexander, D. P. Rowell, E. C. Kent, and A. Kaplan, 2003: Global analyses of sea surface temperature, sea ice, and night marine air temperature since the late nineteenth century. *J. Geophys. Res. Atmos.*, **108**, https://doi.org/10.1029/2002jd002670.

Rogers, J. C., 1981: The North Pacific Oscillation. *J. Climatol.*, **1**, 39–57, https://doi.org/10.1002/joc.3370010106.

Rutz, J. J., and W. J. Steenburgh, 2012: Quantifying the role of atmospheric rivers in the interior western United States. *Atmos. Sci. Lett.*, **13**, 257–261, https://doi.org/10.1002/asl.392.

Shields, C. A., and Coauthors, 2018: Atmospheric River Tracking Method Intercomparison Project (ARTMIP): Project goals and experimental design. *Geosci. Model Dev.*, **11**, 2455–2474, https://doi.org/10.5194/gmd-11-2455-2018.

Taylor, K. E., R. J. Stouffer, and G. A. Meehl, 2012: An overview of CMIP5 and the experiment design. *Bull. Am. Meteorol. Soc.*, **93**, 485–498, https://doi.org/10.1175/BAMS-D-11-00094.1.

Teng, H., and G. Branstator, 2017: Causes of extreme ridges that induce california droughts. *J. Clim.*, **30**, 1477–1492, https://doi.org/10.1175/JCLI-D-16-0524.1.

Thapa, K., T. A. Endreny, and C. R. Ferguson, 2018: Atmospheric Rivers Carry

Accepted for publication in *Journal of Climate*. DOI 10.1175/JCLI-D-22-0089.1.

Nonmonsoon Extreme Precipitation Into Nepal. *J. Geophys. Res. Atmos.*, **123**, 5901–5912, https://doi.org/10.1029/2017JD027626.

Viale, M., R. Valenzuela, R. D. Garreaud, and F. M. Ralph, 2018: Impacts of atmospheric rivers on precipitation in Southern South America. *J. Hydrometeorol.*, **19**, 1671–1687, https://doi.org/10.1175/JHM-D-18-0006.1.

Waliser, D., and B. Guan, 2017: Extreme winds and precipitation during landfall of atmospheric rivers. *Nat. Geosci.*, **10**, 179–183, https://doi.org/10.1038/ngeo2894.

Wallace, J. M., C. Smith, and C. S. Bretherton, 1992: Singular Value Decomposition of Wintertime Sea Surface Temperature and 500-mb Height anomalies. *J. Clim.*, **5**, 561–576.

Woods, C., and R. Caballero, 2016: The role of moist intrusions in winter arctic warming and sea ice decline. *J. Clim.*, **29**, 4473–4485, https://doi.org/10.1175/JCLI-D-15-0773.1.

Xiong, Y., and X. Ren, 2021: Influences of atmospheric rivers on north pacific winter precipitation: Climatology and dependence on ENSO condition. *J. Clim.*, **34**, 277–292, https://doi.org/10.1175/JCLI-D-20-0301.1.

Zhang, P., G. Chen, W. Ma, Y. Ming, and Z. Wu, 2021: Robust atmospheric river response to global warming in idealized and comprehensive climate models. *J. Clim.*, **34**, 7717–7734, https://doi.org/10.1175/JCLI-D-20-1005.1.

Zhang, T., and Coauthors, 2018: Predictability and prediction of Southern California rains during strong El Niño events: A focus on the failed 2016 winter rains. *J. Clim.*, **31**, 555–574, https://doi.org/10.1175/JCLI-D-17-0396.1.

Zhang, W., Z. Wang, M. F. Stuecker, A. G. Turner, F. F. Jin, and X. Geng, 2019: Impact of ENSO longitudinal position on teleconnections to the NAO. *Clim. Dyn.*, **52**, 257–274, https://doi.org/10.1007/s00382-018-4135-1.

Zhou, Y., H. Kim, and D. E. Waliser, 2021: Atmospheric River Lifecycle Responses to the Madden-Julian Oscillation. *Geophys. Res. Lett.*, **48**, 1–10, https://doi.org/10.1029/2020GL090983.

Zhu, Y., and R. E. Newell, 1998: A proposed algorithm for moisture fluxes from atmospheric rivers. *Mon. Weather Rev.*, **126**, 725–735, https://doi.org/10.1175/1520-0493(1998)126<0725:APAFMF>2.0.CO;2.

Accepted for publication in *Journal of Climate*. DOI 10.1175/JCLI-D-22-0089.1.